

LLER Review

Quarterly Report



July–September 1993

Laboratory for Laser Energetics
College of Engineering and Applied Science
University of Rochester
250 East River Road
Rochester, New York 14623-1299



LLE Review

Quarterly Report

Editor: R. J. Hutchison
(716) 275-5772

July–September 1993

Laboratory for Laser Energetics
College of Engineering and Applied Science
University of Rochester
250 East River Road
Rochester, New York 14623-1299



This report was prepared as an account of work conducted by the Laboratory for Laser Energetics and sponsored by New York State Energy Research and Development Authority, the University of Rochester, the U.S. Department of Energy, and other agencies.

Neither the above named sponsors, nor any of their employees, makes any warranty, expressed or implied, or assumes any legal liability or responsibility for the accuracy, completeness, or usefulness of any information, apparatus, product, or process disclosed, or represents that its use would not infringe privately owned rights.

Reference herein to any specific commercial product, process, or service by trade name, mark, manufacturer, or otherwise, does not necessarily constitute or imply its endorsement, recommendation, or favoring by the United States Government or any agency thereof or any other sponsor.

Results reported in the LLE Review should not be taken as necessarily final results as they represent active research. The views and opinions of authors expressed herein do not necessarily state or reflect those of any of the above sponsoring entities.

IN BRIEF

This volume of the LLE Review, covering the period July–September 1993, contains articles on self-focusing of broad-bandwidth laser light with angular dispersion, laser patterning of thin-film circuits, and construction of foam-shell fusion targets. Reports on the detailed designs of major subsystems of the OMEGA Upgrade and on the continuing activation of the upgraded Glass Development Laser system are summarized. Descriptions of research proposals for NLUF are also included in this issue.

Highlights of the research reported in this issue are

- Previous investigations of self-focusing behavior of broad-bandwidth laser light without angular dispersion showed only slight differences when compared to laser light with angular dispersion. A new, numerical investigation of self-focusing with applied angular dispersion shows the development of transverse amplitude modulation, which can act to enhance or impede instantaneous self-focusing. Averaging over one period of phase modulation with imposed bandwidth shows consistent smoothing of the beam, nearly replicating the original spatial profile, including smoothing of induced perturbations due to laser-system imperfections.
- A continuous-wave argon-ion laser beam is focused onto a Y-Ba-Cu-O thin-film circuit. The laser beam selectively heats the epitaxy, which enriches oxygen in irradiated regions alongside depleted regions. Oxygen

enrichment results in the formation of superconducting regions, while oxygen depletion results in semiconducting regions. This maskless operation yields applications in microbridges, coplanar transmission lines, field-effect transistors, and photoconductive switches.

- One technique to form thick fusion fuel layers is to use a low-density polymer or aerosol foam matrix to hold the liquid DT. This issue summarizes the results of a collaborative experiment conducted at the Institute for Laser Engineering (ILE) to fabricate foam-shell targets with plastic-layer overcoats.

CONTENTS

	<i>Page</i>
IN BRIEF.....	iii
CONTENTS	v
Section 1 PROGRESS IN LASER FUSION	193
1.A Numerical Investigation of the Self-Focusing of Broad-Bandwidth Laser Light with Applied Angular Dispersion	193
Section 2 ADVANCED TECHNOLOGY DEVELOPMENTS	209
2.A Laser Patterning of Y-Ba-Cu-O Thin-Film Circuits	209
2.B Fabrication of Foam Shells Overcoated with Plastic Layers	216
Section 3 National Laser Users Facility News	222
Section 4 LASER SYSTEM REPORT	224
4.A GDL Facility Report	224
4.B OMEGA Upgrade Status Report	225
PUBLICATIONS AND CONFERENCE PRESENTATIONS	



Jennifer Traylor and Roman Chrzan, specialists in the Optical Manufacturing Group, monitor application of dielectric thin films on optical elements in the newly installed 72-in. vacuum chamber. This chamber complements two other vacuum chambers in the Optical Manufacturing Department, which will be used to apply optical coatings to the OMEGA Upgrade mirrors, beamsplitters, and polarizers. The 72-in. chamber will be used to coat the largest of the optical components, including the frequency-conversion polarizers and ultraviolet transport mirrors.

Section 1

PROGRESS IN LASER FUSION

1.A Numerical Investigation of the Self-Focusing of Broad-Bandwidth Laser Light with Applied Angular Dispersion

The development and application of beam-smoothing techniques¹⁻⁶ have produced considerable improvement in laser-irradiation uniformity for inertial-confinement fusion (ICF) laser systems. Some of these techniques act passively [e.g., random phase plates (RPP)¹ or distributed phase plates (DPP)²], while others, such as induced spatial incoherence (ISI)³ or smoothing by spectral dispersion (SSD),⁵ are dynamic, calling for the application of broad-bandwidth (BBW) laser light to temporally smooth intensity modulations on target. In this article, we examine the effects of the BBW light used in SSD on the self-focusing of the beam during propagation through nonlinear optical components in the laser system.

The bandwidth used in SSD is in the form of spectrally dispersed, phase-modulated light. Phase modulation is used to minimize the formation of high-intensity spikes that can damage optical materials within the laser system. The spectral angular dispersion serves a dual purpose: it introduces a time-dependent phase variation across the transverse direction of the beam, which leads to intensity smoothing in the far field, and it improves the efficiency of the frequency tripling of the BBW laser light. Both the phase modulation and the angular dispersion enter into the modeling of self-focusing.

Analytic work⁷ has shown that spectrally dispersed, phase-modulated beams develop amplitude modulation as they propagate, but this modulation disappears when the beam is brought to an image plane of the diffraction grating. (These calculations have been validated by experiment.⁸) Such modulation is of

particular concern when the beam is injected into a nonlinear medium, such as a lens or a piece of amplifier glass (rod, disk, etc.), where the threat of self-focusing is always present. There are two features of this amplitude modulation that affect the amount of self-focusing that can occur. First, because the angular dispersion imposed by SSD causes the spectral components to sweep across the beam in time, the average intensity will smooth out over a characteristic modulation time. Second, even though the instantaneous amplitude modulation disappears at appropriate image planes within the laser system, any optical components between these image planes must cope with the instantaneous amplitude modulation on the beam. Laser systems that incorporate SSD to improve beam uniformity would benefit from a thorough understanding of this form of amplitude modulation during propagation in a nonlinear medium.

We have developed a multifrequency, multidimensional computer code to examine the effect of SSD on self-focusing for a beam propagating through a laser system. Results from this computer code indicate that, for a given set of SSD parameters and a nonlinear material, there exists a minimum propagation distance for the amplitude modulation created by SSD to begin self-focusing. For distances greater than this minimum, SSD will further enhance the instantaneous self-focusing when the beam is diverging during image relaying, and it will reduce the self-focusing when the beam is converging. In either case, however, because the spatial positions of the intensity spikes are changing in time, the time-averaged intensity is very smooth when averaged over one modulation period.

Simulation results also indicate that SSD smooths the time-averaged intensity of intrinsic amplitude perturbations produced by optical defects in the laser. This is accomplished by the phase gradients across the beam deflecting the perturbation, as the optical rays propagate in the direction perpendicular to the wavefront. Since the phase variation is time dependent and oscillatory, the perturbation is shifted back and forth across the beam within a period of the modulation frequency. When compared with a monochromatic beam, the time-averaged intensity of the perturbation for SSD is therefore reduced due to its energy being spread out over a larger area.

In this article, we first discuss the numerical approximation used to characterize and model SSD propagation. We then validate the model by (a) reproducing the Bespalov-Talanov (B-T) gain curves for self-focusing in a nonlinear medium, (b) examining a simple test of angular propagation using the Talbot effect, and (c) reproducing the analytic results for SSD propagation in air. Finally, we study BBW propagation and self-focusing in a nonlinear medium.

Numerical Method

The derivation of the SSD technique has been given in detail by Skupsky;⁵ here we highlight the derivation to illustrate the angular dispersion terms. The laser electric field in a nondispersive material can be written in the form

$$E(\mathbf{r}, t) = \Psi(\mathbf{r}, t) e^{i\phi(\mathbf{r}, t)} + c.c. ,$$

where the main contribution to the bandwidth for phase-modulated light is

contained in the time-varying phase term $\phi(\mathbf{r}, t)$, while $\Psi(\mathbf{r}, t)$ represents a more slowly varying pulse-shape term. For the purposes of this calculation, we consider the pulse to be infinitely long and neglect the temporal dependence of Ψ . For sinusoidal phase modulation of the beam, produced by an electro-optic (E-O) crystal, the electric field becomes

$$E(\mathbf{r}, t) = \Psi(\mathbf{r}) e^{i\omega t + i\delta \sin(\omega_m t) - i\mathbf{k} \cdot \mathbf{r}} + \text{c.c.},$$

where δ and ω_m are the modulation amplitude and angular frequency of the modulation and ω and \mathbf{k} are the fundamental angular frequency and wave number of the laser. Spectral dispersion is imposed upon the beam by means of a diffraction grating. Using the relation

$$e^{i\delta \sin(\omega_m t)} = \sum_{j=-\infty}^{\infty} J_j(\delta) e^{i j \omega_m t},$$

the dispersed electric field becomes

$$E(\mathbf{r}, t) = \sum_{j=-\infty}^{\infty} \Psi_j(\mathbf{r}) e^{i(\omega + j\omega_m)t - i k_j z \cos \theta_j} + \text{c.c.},$$

where $\Psi_j(\mathbf{r}) = \Psi(\mathbf{r}) J_j(\delta) e^{-i k_j x \sin \theta_j}$, with spectral dispersion on the x direction.

The wave number is defined as

$$k_j = \frac{n_o}{c} (\omega + j\omega_m),$$

where n_o is the index of refraction, and the angles at which the individual plane waves propagate are determined by the grating dispersion $\Delta\theta/\Delta\lambda$

$$\theta_j = -j\lambda \frac{\Delta\theta}{\Delta\lambda} \frac{\omega_m}{\omega}.$$

To examine self-focusing, we calculate the propagation of this beam through a nonlinear medium using the paraxial approximation to the wave equation. The nonlinearity of the refractive index is represented by writing the index as

$$n = n_o + n_2 \langle E^2 \rangle,$$

where the angle bracket indicates time averaging, and the coefficient n_2 is the index of nonlinearity of the medium. The paraxial equation¹⁰ for a monochromatic plane wave then takes the form

$$2i\bar{k} \frac{\partial \Psi}{\partial z} + \nabla_{\perp}^2 \Psi + 2\bar{k}^2 \left(\frac{n_2}{n_o} \right) |E|^2 \Psi = 0,$$

where $\bar{k} = k_z = |\mathbf{k}| \cos \theta$. Modeling the spectrally dispersed SSD beam requires solving separate equations for each spectral component. However, because of the interfrequency dependency of the four-wave-mixing (4WM) term ($\Gamma \equiv |E|^2 E$) it will be necessary to solve this set of equations simultaneously. For $2N$ spectral components, we have

$$\begin{aligned}
2i\bar{k}_{-N} \frac{\partial \Psi_{-N}}{\partial z} + \nabla_{\perp}^2 \Psi_{-N} + 2\bar{k}_{-N}^2 \left(\frac{n_2}{n_0} \right) \Gamma_{-N} &= 0 \\
& \vdots \\
2i\bar{k}_j \frac{\partial \Psi_j}{\partial z} + \nabla_{\perp}^2 \Psi_j + 2\bar{k}_j^2 \left(\frac{n_2}{n_0} \right) \Gamma_j &= 0 \\
& \vdots \\
& \vdots \\
2i\bar{k}_N \frac{\partial \Psi_N}{\partial z} + \nabla_{\perp}^2 \Psi_N + 2\bar{k}_N^2 \left(\frac{n_2}{n_0} \right) \Gamma_N &= 0.
\end{aligned}$$

where $\Gamma_j = (|E|^2 E)_j$ represents the 4WM contribution to an individual spectral component.

Four-wave mixing refers to the nonlinear process involving three electromagnetic waves interacting to produce a fourth output wave. It is a third-order process and, as such, is governed by the third-order nonlinear susceptibility.¹¹ Two of the input waves form a virtual grating, which scatters the third incident wave into the output. The 4WM processes are divided into three groups: self-, cross-, and mixed-phase modulation. These classifications denote the makeup of the three incident waves. Self-phase modulation, or self-focusing, is one of the more noteworthy 4WM processes. Cross-phase modulation involves a wave reflecting back into itself off a virtual neutral grating produced by another wave and its complex conjugate. In mixed-phase modulation the output wave is almost always the product of three waves with completely different frequencies. To illustrate, we consider the 4WM terms for an electric field consisting of three waves traveling in the same direction $E = E_1 + E_2 + E_3$, with

$$\begin{aligned}
E_1 &= a_0 \exp(i\omega_0 t) \\
E_2 &= a_{-1} \exp[i(\omega_0 - n\omega_m)t] \\
E_3 &= a_1 \exp[i(\omega_0 + n\omega_m)t],
\end{aligned}$$

where the $ik \cdot r$ contribution to the phase has been suppressed. From our general paraxial equation above, we define $\Gamma = |E|^2 E$, where now

$$\Gamma = (E_1 + E_2 + E_3) (E_1 + E_2 + E_3)^* (E_1 + E_2 + E_3).$$

Rewriting, in terms of the exponentials above, we obtain

$$\begin{aligned}
\Gamma &= e^{i\omega_0 t} \left(a_0 + a_{-1} e^{-i\omega_m t} + a_1 e^{i\omega_m t} \right) \left(a_0 + a_{-1} e^{i\omega_m t} + a_1 e^{-i\omega_m t} \right) \\
&\quad \times \left(a_0 + a_{-1} e^{-i\omega_m t} + a_1 e^{i\omega_m t} \right).
\end{aligned}$$

We now expand this relationship and collect terms for individual frequency components. The contributions to the various frequencies are shown in Table 56.I. It can be seen that the 4WM term for a given frequency is dependent on the other frequencies present due to the cross- and mixed-phase modulation terms, in addition to its own self-phase modulation. Also, the three initial waves serve

Table 56.1: Contributions to different harmonics generated by four-wave mixing for the example of three plane waves. Each term is multiplied by an additional factor of $e^{i\omega_0 t}$.

	Self	Cross	Mixed
$e^{-i3\omega_m t}$:			$a_{-1}^2 a_1$
$e^{-i2\omega_m t}$:			$a_{-1}^2 a_0 + 2a_{-1} a_0 a_1$
$e^{-i\omega_m t}$:	a_{-1}^3	$2(a_0^2 + a_1^2)a_{-1}$	$a_0^2 a_1$
1 :	a_0^3	$2(a_{-1}^2 + a_1^2)a_0$	$2a_{-1} a_0 a_1$
$e^{i\omega_m t}$:	a_1^3	$2(a_{-1}^2 + a_0^2)a_1$	$a_0^2 a_{-1}$
$e^{i2\omega_m t}$:			$a_1^2 a_0 + 2a_{-1} a_0 a_1$
$e^{i3\omega_m t}$:			$a_1^2 a_{-1}$

as sources for higher harmonics. This requires that the simulations include a number of higher harmonics whose amplitudes were initially zero.

The simulation code *MCOLORS* is an adaptation of the *MALAPROP*¹² computer code written at Lawrence Livermore National Laboratory. Since *MALAPROP* was written to examine the propagation of a single frequency, a numerical framework was constructed that allows *MCOLORS* to simultaneously propagate all of the frequencies included in an SSD beam. The code propagates each of the individual waves for a spatial step in the z direction and then calculates the coupling terms as described above. A maximum spatial stepsize is determined from the input grid dimensions and the linear and nonlinear refractive indices of the material. The simulation uses finite-difference methods to approximate the paraxial equations and an alternating direction implicit (ADI) numerical scheme to solve the resulting systems of equations. All harmonics were calculated for $|j| \leq 2\delta$, where δ is the modulation amplitude of the E-O crystal. At the grating, the individual wave amplitudes are negligible for harmonics with $|j| \geq \delta$. However, higher harmonics are generated by the 4WM terms during propagation; this is adequately modeled by keeping terms between $\pm 2\delta$.

Verification of Method

Before attempting to model the propagation of a multifrequency laser beam in a nonlinear medium, it was necessary to validate the simulation by reproducing analytic results dealing with self-focusing, angular propagation and SSD propagation in air. Each of these plays a significant role in the propagation of an SSD beam in a nonlinear medium.

1. Monochromatic Self-Focusing in a Nonlinear Medium

The instability of intense laser light propagating within a nonlinear medium has been well established.¹³⁻¹⁵ This effect is often responsible for optical damage to laser-system components and, as such, is a limiting factor in the design of high-power laser systems. Linearized instability theory predicts that small amplitude modulations superimposed on a uniform-intensity background will

grow somewhat exponentially with a gain coefficient g given by¹³

$$g = K \sqrt{\frac{n_2}{n_0} \langle E^2 \rangle - \frac{K^2}{4k^2}},$$

where K is the wave number of the amplitude modulation, n_2 is the nonlinear refractive index, n_0 is the normal index of refraction. $\langle E^2 \rangle$ is the time-averaged value of the electric field, and k is the wave number of the laser. (As noted by Bliss,¹⁶ the growth is not strictly exponential,¹⁷ but such a description does contain all the qualitative features of a complete treatment.) We can rewrite this equation in terms of the background intensity I as

$$g = K \sqrt{\gamma I - \frac{K^2}{4k^2}},$$

where I is measured in GW/cm^2 and γ is a nonlinear coefficient defined as

$$\gamma = \frac{4\pi}{c} \frac{n_2}{n_0} \times 10^{16} \frac{\text{cm}^2}{\text{GW}}.$$

Using this formula for the gain coefficient, it is possible to construct a series of curves, as shown in Fig. 56.1, describing the gain coefficient as a function of the nonlinear coefficient γ for the medium. (Here we have chosen the wave number of the modulation to be 120 cm^{-1} and the laser wavelength as 1053.5 nm .) The individual curves represent three different background intensities (2, 3, and $4 \text{ GW}/\text{cm}^2$). A series of numerical runs were compiled for each intensity over the range of the nonlinear coefficient. The numerical results appear

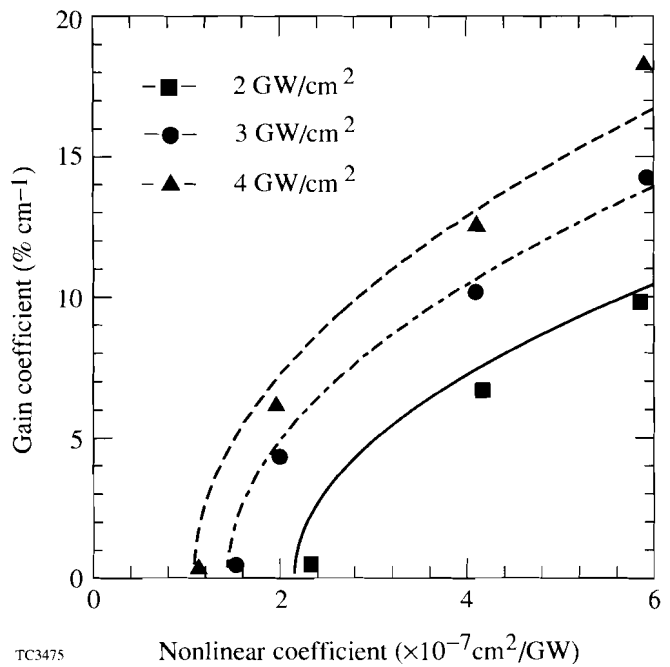
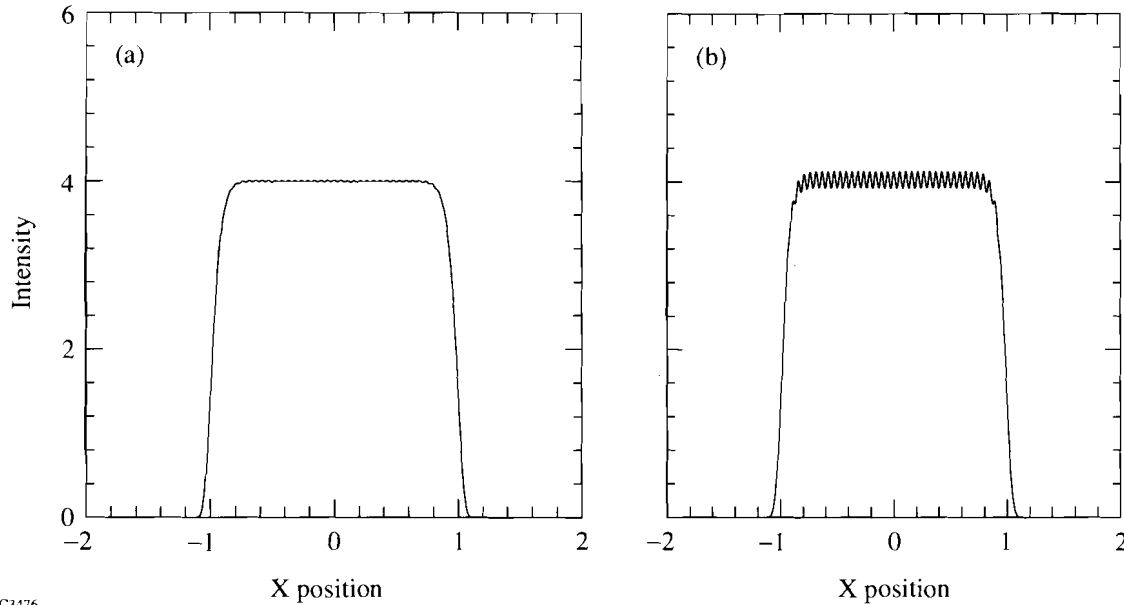


Fig. 56.1 Bepalov-Talanov (B-T) gain coefficient as a function of a nonlinear coefficient γ of the medium. Separate curves are drawn for background intensities of 2, 3, and $4 \text{ GW}/\text{cm}^2$. Numerical simulation results for each case are overlaid.

in Fig. 56.1 as the various symbols overlaid upon the analytic curves. It can be seen that the simulation is in good agreement with the theory. An example of the 4 GW/cm² series is illustrated in Fig. 56.2. The input spatial profile, shown in Fig. 56.2(a), was propagated 25 cm in a nonlinear medium ($\gamma = 4.0 \times 10^{-7} \text{ cm}^2/\text{GW} \sim 10^{-13} \text{ esu}$) and resulted in the growth of the sinusoidal perturbation to that shown in Fig. 56.2(b).



TC3476

Fig. 56.2

Example of the exponential growth of a small sinusoidal intensity modulation on a 4 GW/cm² background. (a) Initial spatial profile; (b) spatial profile after propagating 25 cm in a nonlinear material ($\gamma = 4.0 \times 10^{-7} \text{ cm}^2/\text{GW}$).

2. Angular Propagation

One of the key elements of the SSD method is the imposition of angular dispersion onto the beam. To test that angular propagation was being modeled correctly, we considered solving a simple example of the Talbot effect.¹⁸ Such a test involves the propagation of a field composed of three monochromatic waves traveling in different directions (Fig. 56.3). The Talbot effect maintains that an initial interference pattern in the intensity will repeat itself at distinct positions with uniform spacing along the propagation path. We can determine the location of these positions analytically. The total field is just the summation of the individual plane waves, which we write as

$$E = a_1 e^{-i\mathbf{k}_1 \cdot \mathbf{r}} + a_2 e^{-i\mathbf{k}_2 \cdot \mathbf{r}} + a_3 e^{-i\mathbf{k}_3 \cdot \mathbf{r}},$$

where

$$\mathbf{k}_1 \cdot \mathbf{r} = kz \cos \theta + kx \sin \theta$$

$$\mathbf{k}_2 \cdot \mathbf{r} = kz$$

$$\mathbf{k}_3 \cdot \mathbf{r} = kz \cos \theta - kx \sin \theta .$$

Setting $a_1 = a_3 = 1/4$ and $a_2 = 1/2$, we obtain

$$E = \frac{1}{2} \left[e^{-ikz \cos \theta} \cos(kx \sin \theta) + e^{-ikz} \right].$$

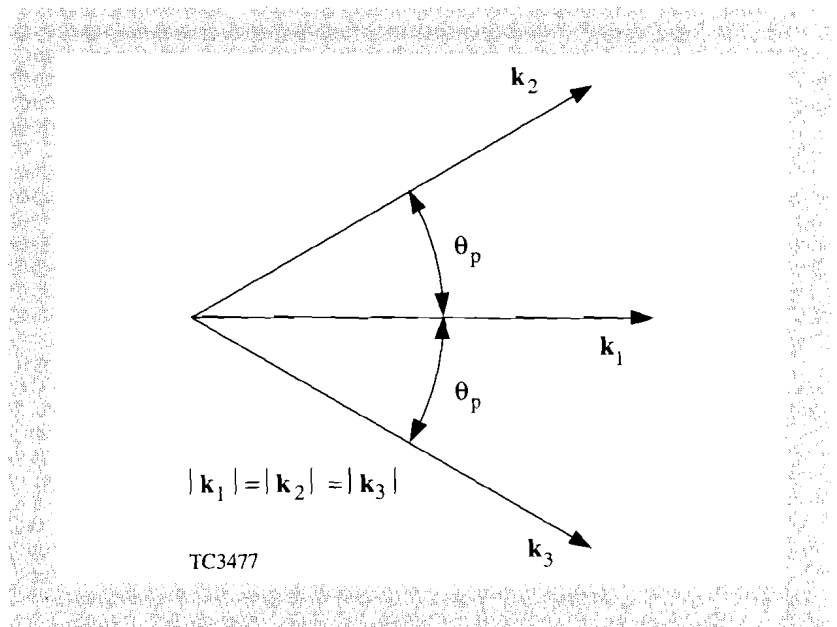


Fig. 56.3
Wave-vector alignment for a three-wave angular propagation test. All three-wave numbers are equal, but \mathbf{k}_2 and \mathbf{k}_3 are traveling at angles $\pm\theta_p$ from \mathbf{k}_1 as shown.

Initially ($z = 0$), and at various positions along the propagation path, the two exponential factors will have the same value. This occurs for the condition $kz \cos \theta + 2\pi n = kz$, yielding

$$z = \frac{n\lambda}{(1 - \cos \theta)} \quad n = 0, 1, 2, \dots$$

At these positions the intensity is given by

$$I = |E|^2 = \cos^4 \left(\frac{kx}{2} \sin \theta \right).$$

The intensity pattern for the values $\lambda = 1053.5 \text{ nm}$ and $\theta = 5.0 \times 10^{-4} \text{ rad}$ is shown in Fig. 56.4(a). We now consider the propagation distance at which the two phase terms above become 90° out-of-phase

$$\left[kz \cos \theta + \left(\frac{2n-1}{2} \right) \pi = kz \right].$$

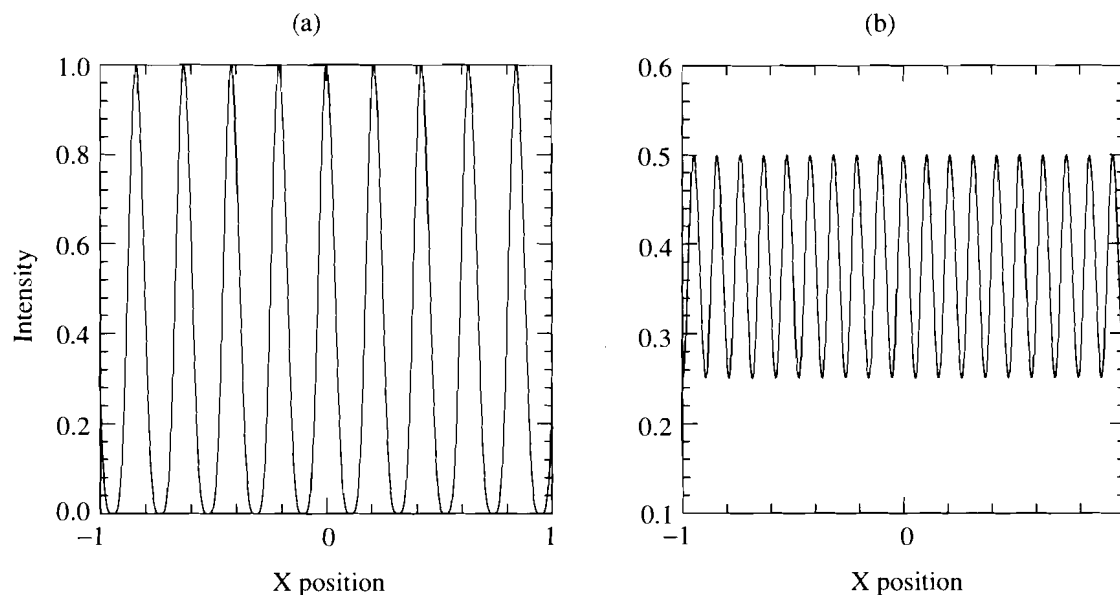
This leads to

$$z = \left(\frac{2n-1}{4} \right) \frac{\lambda}{(1 - \cos \theta)} \quad n = 0, 1, 2, \dots$$

with the intensity at these positions given by

$$I = \frac{1}{4} \left[\cos^2(kx \sin \theta) + 1 \right].$$

Therefore, if we propagate to the position given by this expression for $n = 1$, we should see a modulated intensity with a maximum intensity of $1/2$, a minimum intensity of $1/4$, and a spatial wavelength $1/2$ the value from the previous example. We calculate the necessary propagation distance to be



TC3478

Fig. 56.4
 Spatial intensity profiles for a three-wave angular propagation test. (a) Initial ($z = 0$) interference pattern. All three wavelengths are equal to 1053.5 nm, and the propagation angles are $\pm 5.0 \times 10^{-4}$ rad; (b) numerically calculated intensity profile at a propagation distance of $z = 210.7$ cm. The features of this profile agree well with the analytic predictions.

$z = 210.7$ cm. The result of an *MCOLORS* run, using these parameters, is shown in Fig. 56.4(b). From this graph it can be seen that the simulation is in good agreement with the analytic result.

3. SSD Propagation in Air

The last test we examine is modeling the propagation of an SSD beam in air. This problem has been solved previously in an analytic model.⁷ This work, verified in experiments,⁸ showed that the spectral angular dispersion causes SSD beams to develop amplitude modulation during propagation. As the wavefronts propagate, they become spatially modulated in the transverse direction. This modulation, because of the time-dependent phase, sweeps spatially across the beam in time on successive wavefronts. Picking out a specific point in the propagation path, the analytic model examines the intensity moving past that point as a function of time. Typical results of the analytic model are shown in Fig. 56.5(a). The unperturbed beam started at $z = 0$ and was propagated 5 m with an E-O modulator frequency of 10 GHz, a modulation amplitude of 4, and a dispersion coefficient due to a diffraction grating of 200 mm/Å. The same parameters were used in an *MCOLORS* simulation to produce the set of amplitude functions (Ψ_j) at the propagation distance of 5 m. The phase terms of the individual spectral components

$$\left[e^{i(\omega_m t - \hat{k}_m z)} \right]$$

of the total electric field were then evaluated in time at a single transverse position of the beam. Comparison of this result [Fig. 56.5(b)] with the analytical result indicates that there is good agreement between the two in predicting the amplitude and period of the intensity modulation.

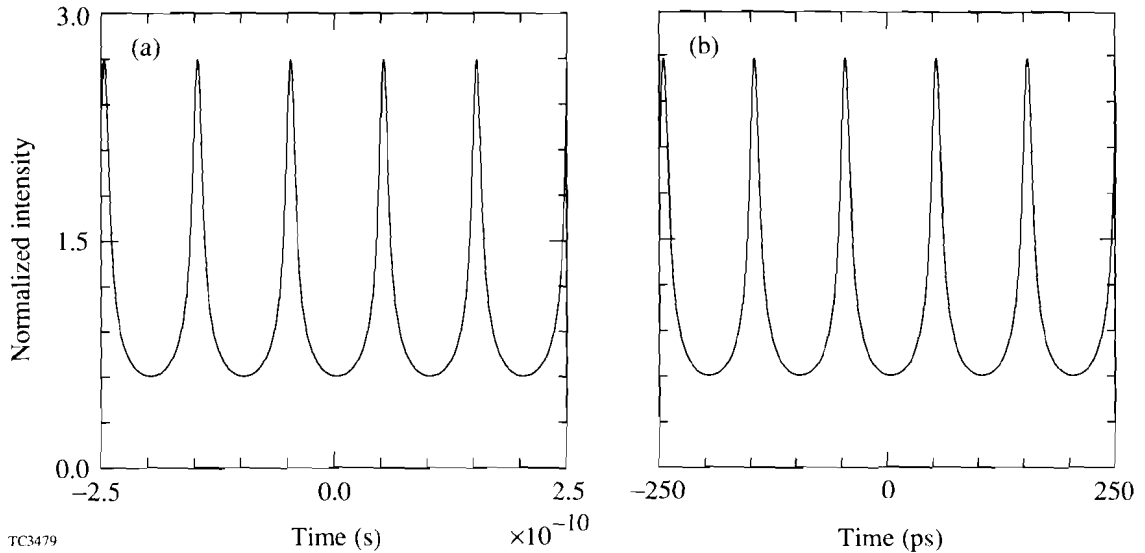


Fig. 56.5

Comparison of analytical calculations and numerical results detailing the accumulated amplitude modulation due to SSD propagation over 5 m. This case involved a modulation frequency of 10 GHz, a modulation amplitude of 4, and a grating dispersion coefficient of $200 \mu\text{m}/\text{\AA}$. (a) Results of the analytic model; (b) results of the numerical simulation.

Propagation of Angularly Dispersed, BBW Light in a Nonlinear Medium

Using the methods described above, we can now examine the propagation and self-focusing characteristics of an SSD beam in a nonlinear medium. We examine two separate scenarios involving phase- and amplitude-modulated beams injected into a nonlinear medium. The first scenario deals with an SSD beam that has developed amplitude modulation solely as a result of propagation. The second scenario involves the study of an SSD beam with an imposed frequency-independent amplitude perturbation on the beam, presumably the result of laser system imperfections.

1. Self-Focusing of Modulation due to Propagation

The self-focusing behavior of an SSD beam as it propagates in a nonlinear material is more easily characterized when the amplitude modulation is allowed to grow to a point where the self-focusing becomes prevalent. There is a critical path length for a given set of SSD and nonlinear material parameters at which self-focusing will begin to occur. As shown in Fig. 56.1, self-focusing occurs when the modulated spikes reach a minimum intensity for a given nonlinear coefficient. Below this value, diffraction will dominate, and the energy in the spike will spread out. A numerical analysis was performed to determine the propagation length required to modulate an SSD beam to such a point that, when injected into a nonlinear medium, self-focusing would begin to occur at a rate of $0.5\% \text{ cm}^{-1}$. Using this criterion, we have produced three curves (shown in Fig. 56.6) that illustrate the dependence of the critical path length as a function of the modulation frequency for several cases of bandwidth (3 \AA , 9 \AA , and 18 \AA). (For this set of curves we have chosen the nonlinear coefficient to be $\gamma = 2.9 \times 10^{-7} \text{ cm}^2/\text{GW}$ and the dispersion coefficient to be $200 \mu\text{m}/\text{\AA}$.) From the graph, it can be seen that as one moves to more extreme conditions for SSD (i.e., more bandwidth and higher modulation frequencies), the critical path length gets shorter and shorter. This is due to the shrinking of the transverse

spatial wavelength of the phase modulation in these cases. Since the optical ray propagation is in the direction perpendicular to the wave front, as the gradients in the wave front become steeper, energy within the beam will be pushed into spikes more quickly, and the beam will experience amplitude modulation over a shorter propagation distance.

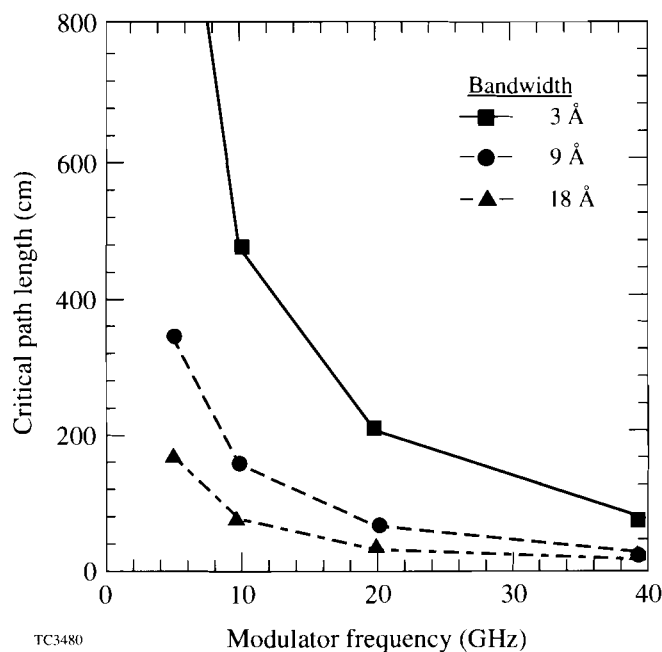


Fig. 56.6
Critical propagation path length for self-focusing (B-T gain coefficient of $0.5\% \text{ cm}^{-1}$) as a function of modulator frequency for three separate values of bandwidth (3 Å, 9 Å, and 18 Å).

Using this information, we now propagate a beam a distance greater than its critical path length to observe the effects of SSD on self-focusing. In addition, it should be remembered that since a laser beam is image-relayed as it propagates through a laser system, it is possible that the SSD beam will sample nonlinear material while it is propagating away from (diverging) or toward (converging) an image plane. To examine the difference this has on self-focusing, an unperturbed beam was imposed with 3-Å bandwidth, an E-O modulation frequency of 10 GHz, and a grating dispersion of $200 \mu\text{m}/\text{Å}$. The initial relative phase distribution is given in Fig. 56.7(a). The beam was then propagated a distance of 550 cm, which resulted in the spatially modulated profile shown in Fig. 56.7(b). Using this profile, we examined the differences in self-focusing over a distance of 50 cm between a diverging SSD beam, a monochromatic beam, and a converging SSD beam. The results of these runs are shown in Fig. 56.8. The monochromatic beam results [Fig. 56.8(b)] serve as a reference for the nominal amount of self-focusing possible. In the case of the diverging SSD beam [Fig. 56.8(a)] it can be seen that the spatial redistribution of the beam energy into spikes due to SSD enhances the overall self-focusing. On the other hand, the converging SSD beam [Fig. 56.8(c)] removes energy out of the spikes and, as such, reduces the amount of self-focusing that takes place. The maximum intensity of the spikes in Fig. 56.8(c) is noticeably lower than the monochromatic reference case in Fig. 56.8(b).

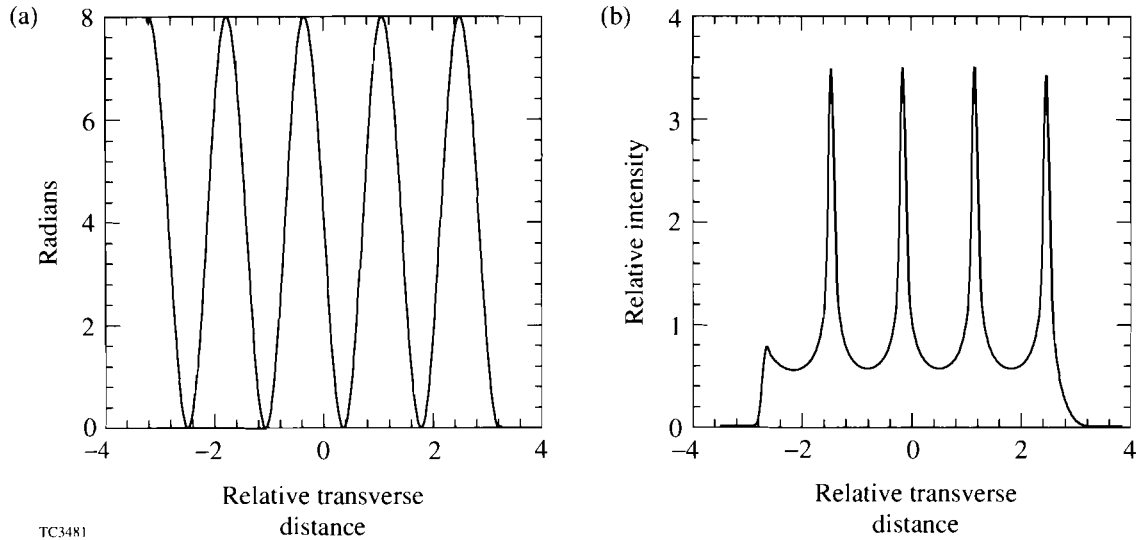


Fig. 56.7
 Spatial intensity profile used in examining the effects of SSD on self-focusing in a nonlinear medium. (a) Initial spatial profile of the relative phase distribution across the beam; (b) modulated intensity profile after propagating 550 cm.

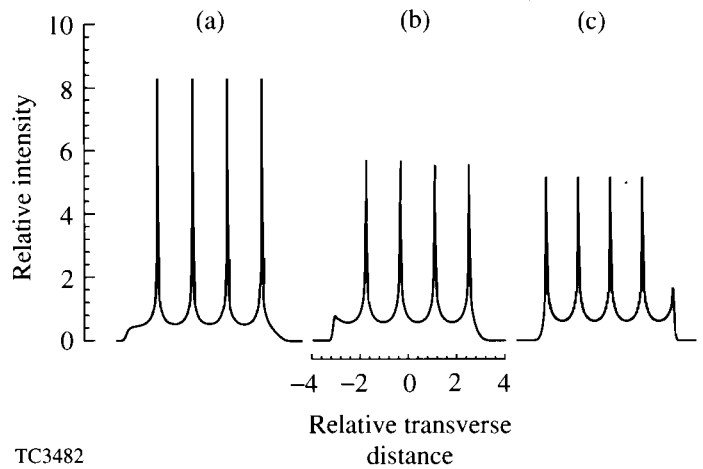


Fig. 56.8
 Comparison of self-focused intensity profiles due to monochromatic and converging and diverging SSD beams in a nonlinear medium. (a) Intensity profile due to a diverging SSD beam; (b) intensity profile due to a monochromatic beam; (c) intensity profile due to a converging SSD beam.

These results represent instantaneous modulation development along a wave front propagating through the system. However, it is important to remember that the phase modulation, and hence the resultant amplitude modulation, is time dependent. The transverse position of an amplitude spike will be shifted on succeeding wave fronts. As such, the spikes will smooth out when the intensity is averaged over one E-O modulation period. An example of this smoothing will be shown in the next subsection.

2. Intrinsic Sources of Amplitude Modulation

The last situation to examine is when an SSD beam samples a defect in the laser system that serves as a source of additional intensity perturbations. Of interest is whether the presence of SSD serves to enhance or reduce the amount of self-focusing that these perturbations would suffer upon injection into a nonlinear material. To examine this problem, we first initialize an SSD beam with a well-defined amplitude spike [as shown in Fig. 56.9(a)] and then propagate it in air. (Here we have assumed that the defect produces the same percentage amplitude modulation for each spectral component.) Of particular importance is the spatial alignment of the amplitude spike with the phase distribution of the SSD beam given in Fig. 56.9(b). Depending on the phase distribution at the amplitude spike, energy can be directed into or out of the spike, and the whole spike can be deflected as the wave propagates. (This is due again to optical ray propagation perpendicular to the wave front.) The defect will be deflected from side to side as the gradient in phase across it alternates its direction in time. This gives the impression of the intensity spike sweeping spatially in time with a period equivalent to that of the E-O modulation frequency. This excursion about the original axial location of the defect results in the time-averaged intensity being lower than the initial defect intensity. Figure 56.10 illustrates this effect.

The profile shown in Fig. 56.9(a) was propagated 300 cm and resulted in the profile given in Fig. 56.10(a). It can be seen that the background intensity has suffered the usual modulation due to SSD propagation. At this particular time,

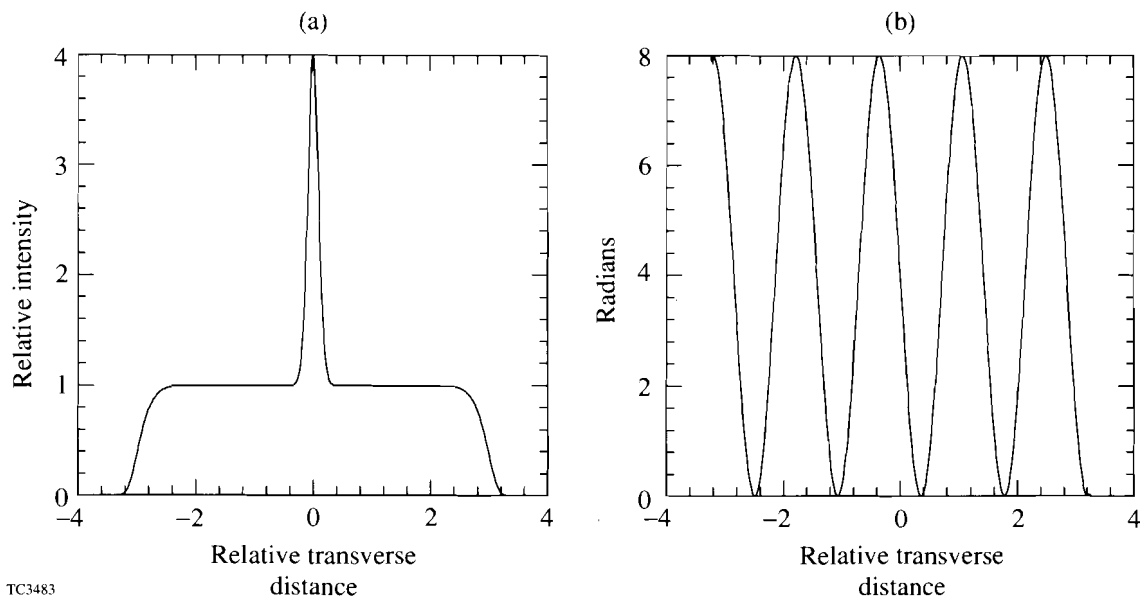


Fig. 56.9

Spatial intensity profile used to examine the effects of SSD on the self-focusing of intrinsic amplitude modulation within a laser system. (a) Initial intensity profile with a 4-to-1 spike modulation; (b) spatial profile of the SSD relative phase distribution sampling the intrinsic spike modulation.

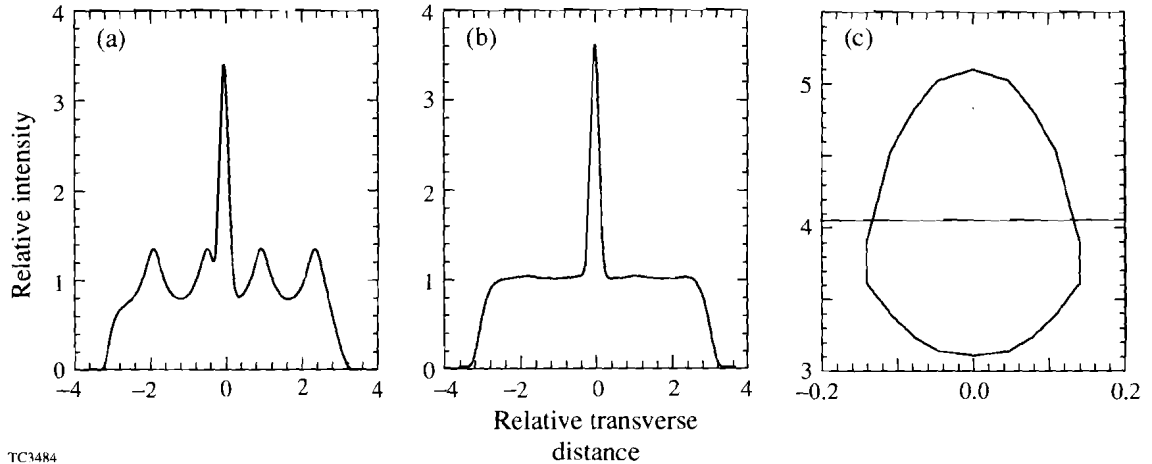
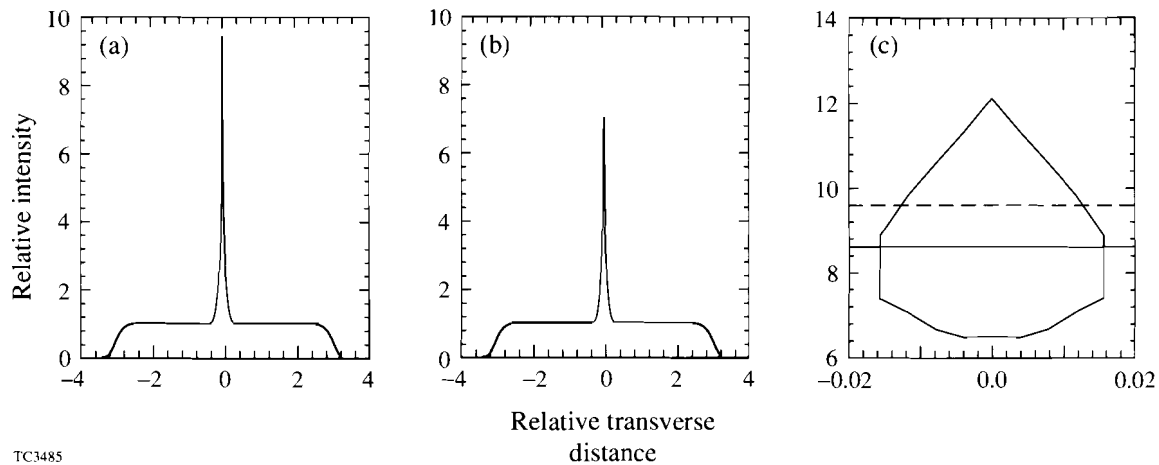


Fig. 56.10

Intensity profiles due to SSD propagation in air for 300 cm. (a) Instantaneous intensity profile. Note the modulated background and reduced and spatially shifted peak. (b) Time-averaged intensity profile after one period of the modulation. The background amplitude modulation has been smoothed, and the peak intensity has been reduced from an initial value of 4. (c) Excursion map of the peak intensity as a function of its spatial position over a single period of the modulation frequency. The solid horizontal line represents an effective peak intensity for the excursion period.

the intensity of the initial spike has been reduced, while its position has been shifted left of the original defect location in the center of the beam. A series of runs were compiled for several times during a single period of the E-O modulator frequency to generate the time-averaged intensity shown in Fig. 56.10(b). Two important features can be seen from this graph. First, as was indicated earlier, the instantaneous modulation of the background intensity due to SSD propagation has been smoothed over the E-O period. Second, the time-averaged intensity of the spike has been reduced to a level lower than its original value. This second point can be explained by examining an excursion map of the spike intensity as a function of its deflected spatial position [Fig. 56.10(c)]. We take the average intensity contribution of the spike at each position in Fig. 56.10(c) to determine an effective spike intensity during the period. This effective intensity is represented by the horizontal line drawn across the graph in Fig. 56.10(c). (The actual dependence is parabolic, is centered at the origin, and has a 10% peak-to-valley variation.) In this case it can be seen that the effective intensity is equal to the initial defect intensity. The lower average intensity is then due to this effective intensity sweeping back and forth across the excursion region during a simple period. Although the time-averaged intensity is lower than the original defect intensity, the excursion map shows that the magnitude of the instantaneous intensity can, at times, be greater than that of the original perturbation. This is the case when the position of the initial defect spike becomes subject to growth due to the SSD propagation modulation.

Knowing the behavior of the beam in air, we can now examine the problem of the beam propagating in a nonlinear material. The profile given in Fig. 56.9(a) was propagated 70 cm in a nonlinear medium ($\gamma = 2.9 \times 10^{-7} \text{ cm}^2/\text{GW}$) with the results shown in Fig. 56.11. Figure 56.11(a) shows a reference monochromatic beam in which the defect spike has experienced more than a factor-of-2 increase in intensity. A series of runs were again compiled for the SSD beam for many times during a single period of the modulator. The averaged results, shown in Fig. 56.11(b), indicate that the self-focused SSD beam has an average intensity that is lower than the reference monochromatic case. Examining the excursion



TC3485

Fig. 56.11

Intensity profiles due to SSD propagating 70 cm in a nonlinear material ($\gamma = 2.9 \times 10^{-7} \text{ cm}^2/\text{GW}$). (a) The self-focused intensity profile due to the propagation of a monochromatic beam. The initial peak intensity of 4 has more than doubled at this point. (b) Time-averaged, self-focused intensity profile due to an SSD beam. While the SSD beam has experienced self-focusing, its magnitude is less than the monochromatic case above. (c) Excursion map of the peak self-focused intensity over a single period of the modulation frequency. The dotted line indicates the value of the peak self-focused intensity given in (a). The solid line represents an effective peak intensity for the excursion period.

map [Fig. 56.11(c)], we have added a dotted horizontal line that indicates the value of the self-focused monochromatic beam. It should be noticed that the effective spike intensity (solid line) is lower than this value. This difference is due to the nonlinear response of the medium. When the spike intensity is reduced due to SSD laterally shifting its energy away, it has far less opportunity to self-focus than in the case of when SSD shifts energy into the spike. While the latter case yields an instantaneous self-focused intensity that is greater than the monochromatic case, the combination of the two, because the lower value has not kept pace, gives an effective intensity that is lower than the monochromatic case. As before, the average intensity is lower than the effective intensity due to the effective intensity sweeping over the excursion region. Finally, we have propagated a distance for the beam to exhibit a respectable amount of self-focusing but with only a modest amount of instantaneous propagation modulation. However, as in the case for air, one can expect that any amount of this type of modulation will smooth out over the E-O modulation period.

Conclusions

The need for good irradiation uniformity in ICF target implosions has led to the development and application of several beam-smoothing techniques that employ BBW light. In conjunction with BBW light, SSD applies spectral angular dispersion to produce smooth beam envelopes in the target plane. While SSD produces very smooth beams over times comparable to the E-O modulation frequency, the beams may develop instantaneous amplitude modulation as they propagate through the laser system. The understanding of how such beams behave as they propagate within the nonlinear media of the laser can be important to prevent damage in glass components.

We have developed a multidimensional, multifrequency computer code to examine the propagation of a BBW beam with applied angular dispersion through a laser system. Results from this computer simulation indicate that, for a given set of SSD parameters and nonlinear material, the SSD beam must be propagated a minimum threshold distance before self-focusing (defined as a gain

coefficient of $0.5\% \text{ cm}^{-1}$) of its modulation will occur. For distances greater than this minimum, SSD will further contribute to self-focusing when the beam is diverging during image relaying and will reduce the self-focusing when the beam is converging. However, in both cases, the time-averaged intensity is very smooth when averaged over one E-O modulation period.

Simulation results indicate that for imposed amplitude perturbations due to laser imperfections, the SSD beam will, at times, yield a peak instantaneous perturbed intensity that exceeds either the initial perturbed intensity in the case of propagating in a linear material or the self-focused intensity of a similarly perturbed monochromatic beam in the case of propagating in a nonlinear material. In both cases, however, results confirm the time-averaged perturbed intensity is reduced during propagation by the presence of SSD on the beam.

ACKNOWLEDGMENT

This work was supported by the U.S. Department of Energy Office of Inertial Confinement Fusion under Cooperative Agreement No. DE-FC03-92SF19460, the University of Rochester, and the New York State Energy Research and Development Authority. The support of DOE does not constitute an endorsement by DOE of the views expressed in this article.

REFERENCES

1. Y. Kato *et al.*, Phys. Rev. Lett. **53**, 1057 (1984).
2. T. Kessler *et al.*, LLE Rev. **33**, 1 (1987).
3. R. H. Lehmburg, A. J. Schmitt, and S. E. Bodner, J. Appl. Phys. **62**, 2680 (1987).
4. R. S. Craxton, S. Skupsky, and J. M. Soures, LLE Review **36**, 158 (1988).
5. S. Skupsky, R. W. Short, T. Kessler, R. S. Craxton, S. Letzring, and J. M. Soures, J. Appl. Phys. **66**, 3456 (1989).
6. R. W. Short and S. Skupsky, IEEE J. Quantum Electron. **26**, 580 (1990).
7. R. W. Short (private communication).
8. T. Kessler (private communication).
9. A. Yariv, *Quantum Electronics*, 2nd ed. (Wiley, New York, 1975), Sec. 14.4.
10. L. A. Vainshtein, Sov. Phys.-Tech. Phys. **9**, 157 (1964).
11. Y. R. Shen, *The Principals of Nonlinear Optics* (Wiley, New York, 1984), p. 242.
12. W. W. Simmons, J. T. Hunt, and W. E. Warren, IEEE J. Quantum Electron. **QE-17**, 1727 (1981).
13. V. I. Bespalov and V. I. Talanov, JETP Lett. **3**, 307 (1964).
14. J. R. Jokipii and J. Marburger, Appl. Phys. Lett. **23**, 696 (1973).
15. A. Campillo, S. L. Shapiro, and B. R. Suydam, Appl. Phys. Lett. **24**, 178 (1974).
16. E. S. Bliss *et al.*, Appl. Phys. Lett. **25**, 448 (1974).
17. S. A. Akhmanov, R. V. Khokhlov, and A. P. Sukhorukov, in *Laser Handbook*, edited by F. T. Arecchi and E. O. Schulz-Du Bois (North Holland, Amsterdam, 1972), p. 1168.
18. H. F. Talbot, Lond. and Edin. Phil. Mag. and J. of Sci., Vol. 9, **56**, 401 (1836).

Section 2

ADVANCED TECHNOLOGY DEVELOPMENTS

2.A Laser Patterning of Y-Ba-Cu-O Thin-Film Circuits

In this article studies on electrical properties of Y-Ba-Cu-O test circuits fabricated using a laser-patterning technique are reported. Laser patterning implements a focused beam from a cw Ar-ion laser to selectively heat up an epitaxial Y-Ba-Cu-O film in a controlled (oxygen or oxygen-free) atmosphere. Local heating enables oxygen to diffuse in or out (depending on the outside atmosphere) of the laser-annealed lines and form oxygen-rich (superconducting) regions next to oxygen-depleted (insulating at low temperature) ones. The procedure is noninvasive, does not require a patterning mask, and does not contaminate or damage the surface of patterned films. Our laser-written, oxygen-rich lines (typically 4 μm to 60 μm wide) possess excellent superconducting properties with zero resistivity at 90 K and critical current densities of above 2 MA/cm^2 at 77 K. On the other hand, oxygen-poor regions are semiconducting and exhibit at low temperatures thermally activated transport, well described by a three-dimensional, variable-length hopping process. Their resistance below 100 K is above 10 MW/square. A number of test structures patterned by laser writing, such as a microbridge, coplanar transmission line, open-ended microwave resonator, photoconductive switch, and Y-Ba-Cu-O field-effect transistor, have been presented.

Planar patterning of $\text{YBa}_2\text{Cu}_3\text{O}_{7-x}$ (YBCO) thin films is one of the key technological issues that must be resolved before successful fabrication of even moderately complex, high- T_c superconducting circuits will be possible.¹ YBCO is a multielement material with highly anisotropic crystalline structure,

which makes the etching process difficult and often results in patterns with fuzzy edges and a degraded (e.g., oxygen-deficient) chemical composition. The problem is especially important in few-micron-wide circuits intended for very high current density and/or high-frequency applications since damaged, oxygen-depleted edges severely limit the structure's supercurrent-carrying capabilities and produce excessive RF losses.² In addition, the YBCO surface is extremely sensitive to contamination by chemicals used in standard patterning procedures.

Micropatterning techniques, suitable for YBCO thin-film circuits, usually represent a combination of photolithography and various wet/dry-etching processes.¹ So far, the most successful is ion milling, which allows one to fabricate structures with submicrometer dimensions. Unfortunately, the ion-milling process requires a photomask and expensive vacuum equipment, and it often leads to patterns with partially oxygen-depleted edges. Laser ablation is also a convenient dry-etching technique. The method is fast and requires no patterning mask or any protection of the YBCO surface. However, it produces patterns "sprinkled" with ablated debris, and its practical applicability is limited to rather simple and undemanding structures.³

Recently a new laser method for patterning YBCO circuits was demonstrated.⁴⁻⁸ The technique is based on the observation that YBCO electrical and optical properties are very sensitive to the material's oxygen content. Oxygen can be diffused in or out of the YBCO film by heating the sample in either the presence or the absence of an oxygen atmosphere. The heating can be done locally with a focused laser beam. Thus, an intentionally oxygen-depleted (insulating at low temperatures) YBCO film can be patterned by embedding in it oxygen-rich (superconducting) lines or vice versa. The writing is fully reversible, and the patterns can be either erased by furnace annealing or rewritten by subsequent laser writing. Most importantly, the technique is noninvasive, requires no patterning mask, and results in completely planar structures, free of surface contamination or edge degradation.

The aim of this article is to demonstrate that the laser-writing method is a reliable and practical technique, perfectly suited for patterning even complicated YBCO thin-film devices and circuits. We examine several laser-written test devices and show that they exhibit excellent superconducting properties and can survive, without degradation, long-term storage in air at room temperature. Some of them also combine in a new and unique way the superconducting and dielectric properties of the oxygen-rich and oxygen-poor YBCO phases. These latter structures are, in our opinion, prime candidates for the proposed high- T_c superconducting optoelectronics.⁹

Figure 56.12 presents a block diagram of our laser-patterning apparatus. The system consists of an Ar-ion cw laser ($\lambda = 0.514 \text{ mm}$), shutter, focusing microscope, and computer-controlled X-Y translational stage with a gas chamber and sample holder. The sample ambient atmosphere is either pure nitrogen or oxygen. Contrary to our previous arrangement,⁸ the substrate of the YBCO film is not in a direct heat contact with the metallic substrate holder, but it is suspended on a thin thermal insulator. This change allowed us to reproducibly write two-dimensional patterns not only on YBCO-on-LaAlO₃ films but also on films

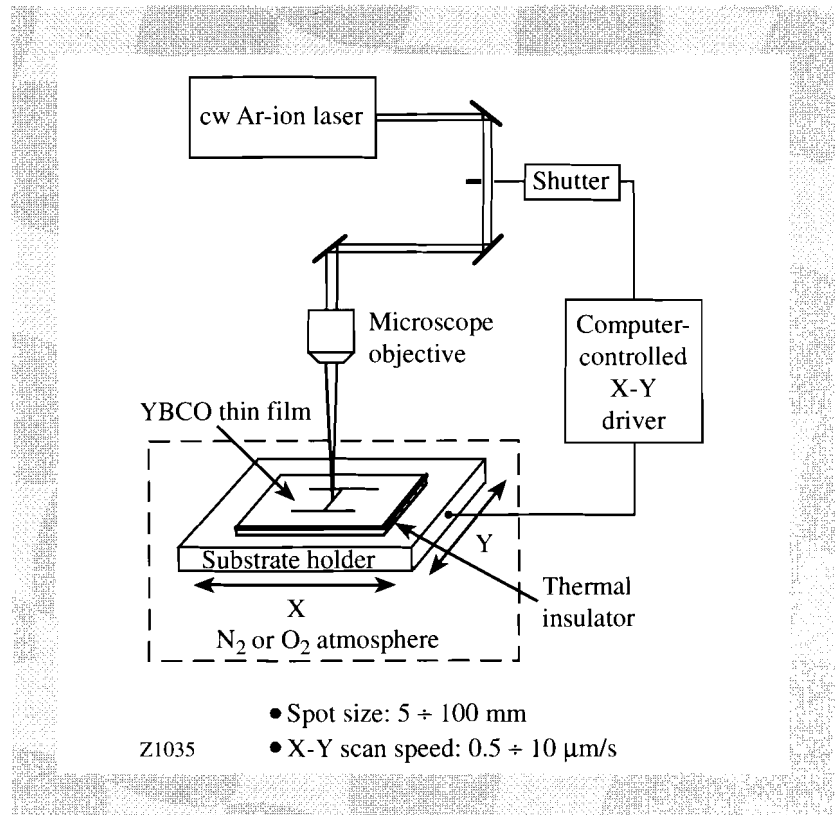


Fig. 56.12
 Block diagram of a two-dimensional laser-patterning apparatus.

deposited on MgO and SrTiO₃. Simultaneously, it eliminated the previously considered need to implement a substrate heater. Typical line dimensions of our patterns varied from $<5 \mu\text{m}$ to $100 \mu\text{m}$. Laser-power intensity applied to the film was kept between 0.2 and $5 \text{ mW}/\mu\text{m}^2$, and a translational stage speed was in the range of 0.5 to $5 \mu\text{m/s}$ for writing oxygen-rich lines and $\sim 50 \mu\text{m/s}$ for (written in nitrogen) oxygen-poor structures.

Our test structures were laser patterned on about 200- to 300-nm-thick epitaxial YBCO films, grown using a single-target RF sputtering technique.¹⁰ The best as-deposited films exhibited about 0.5-K-wide (10%–90%) superconducting transition ΔT_c with the zero resistivity T_{c0} at 89.5 K, and the critical current density J_c of above $2 \text{ MA}/\text{cm}^2$ at 77 K. The films have been intentionally deoxygenated by radiative heating for 60 min in 15 mTr of argon at 680°C to become nonsuperconducting. Indeed, after the argon annealing, their sheet resistance below 100 K was above $10 \text{ M}\Omega/\text{square}$, which represented the upper limit of our resistance-measurement apparatus. Figure 56.13(a) shows the resistance-versus-temperature $R(T)$ curve for one of our oxygen-depleted films. We see that the film resistance rapidly increases at low temperatures, quickly reaching our $20\text{-M}\Omega$ measurement limit. The observed behavior is characteristic for a thermally activated transport in disordered semiconductor materials, as illustrated in Fig. 56.13(b), where the $\ln[R(T)/R(300 \text{ K})]$ dependence is plotted as a function of the fourth root of the inverse temperature. We note that most of our experimental data points follow a straight line, demonstrating that the low-temperature transport in oxygen-poor YBCO is controlled by three-dimensional, variable-length hopping.¹¹

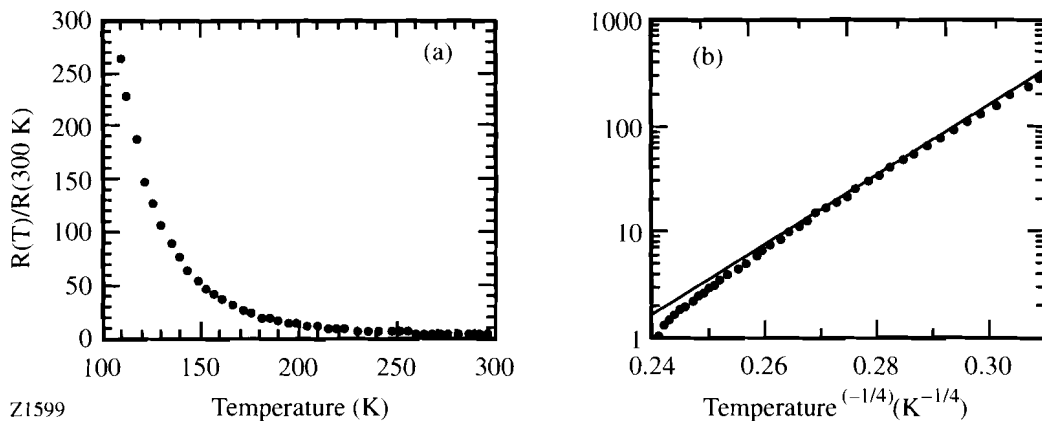


Fig. 56.13 Resistive behavior of an ~200-nm-thick YBCO-on-LaAlO₃ film. (a) Linear $R(T)/R(300\text{ K})$ dependence and (b) logarithmic $R(T)/R(300\text{ K})$ dependence versus the fourth root of the inverse temperature. The film room temperature resistance $R(300\text{ K}) \approx 75\text{ k}\Omega$.

Optical micrographs of four laser-written test structures are shown in Fig. 56.14. All devices are fully monolithic and exhibit very sharp (less than 1 μm wide) superconducting-semiconducting interfaces with linear current-voltage characteristics.¹² Figure 56.14(a) shows a 7- μm -wide microbridge designed for ultrafast optical response measurements,^{9,13} as well as for $R(T)$ and $J_c(T)$ tests as discussed later. Figure 56.14(b) presents a 10- μm -wide, oxygen-poor YBCO photoconductive switch incorporated into a coplanar transmission line. The structure is similar to that of a GaAs photoconductive switch (so-called “Auston switch”), routinely used in generating ultrafast electrical transients,¹⁴ and is intended for our studies of the dynamics of electron-hole pair generation in semiconducting YBCO. It is also expected to find applications as an electrical pulse generator in HTS optoelectronic circuits.¹⁰ Figure 56.14(c) shows one end of an open-ended coplanar microwave resonator. The resonator is incorporated

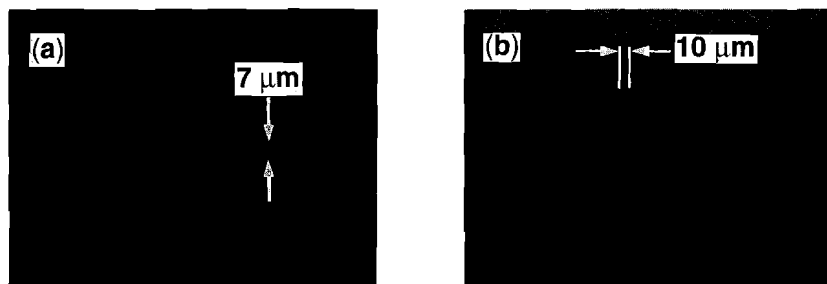
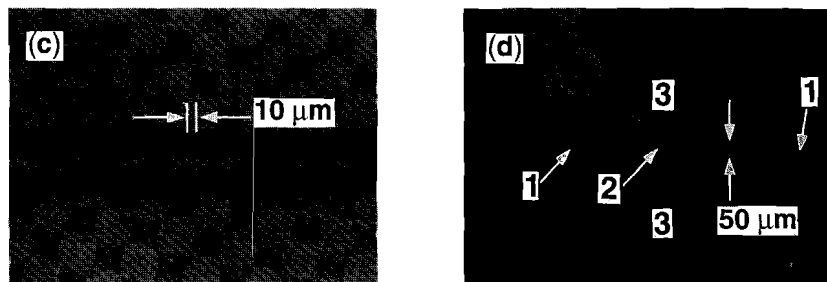


Fig. 56.14 Optical transmission micrographs of oxygen-rich (dark) test structures, laser written on oxygen-depleted (semitransparent) YBCO films. (a) 7- μm -wide and 160- μm -long microbridge; (b) 10- μm -wide oxygen-poor photoconductive switch incorporated into a superconducting coplanar transmission line; (c) left end of an open-ended coplanar microwave resonator; and (d) field-effect test structure prepared in a single YBCO film (gate electrode not shown).



Z1598

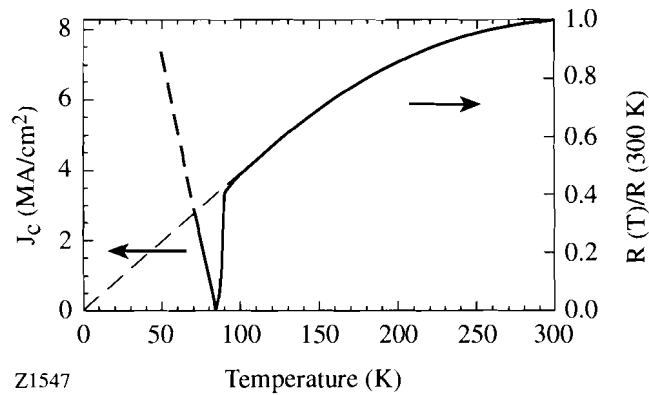


Fig. 56.15
Resistance and critical current density dependence on temperature for the microbridge shown in Fig. 56.14(a).

into a coplanar transmission line. Its 10- μm -wide coupling slit was patterned by overwriting the oxygen-rich line in N_2 atmosphere. A resonator structure identical to that shown in Fig. 56.14(c) but with the line separation of 285 μm has been tested and has shown very good microwave properties. Its quality factor measured at 24 K was about 5000 at 6.5 GHz, and we observed more than 60-dB improvement in the coplanar-line-transmitted power S_{21} in the frequency range of 1 to 15 GHz, as the temperature was lowered from 300 K to that below T_c . At all temperatures below T_c , the S_{21} was near 0 dB, indicating low microwave losses of the oxygen-poor YBCO.¹⁵ These findings clearly demonstrate applicability of our laser-patterning technique for fabricating microwave circuits and devices. Finally, Fig. 56.14(d) presents a top view of a YBCO electric-field device with a partially deoxygenated channel. The homogeneous regions with three different levels of gray, visible in this figure, correspond to (1) highly oxygenated drain and source (the two dark regions; $T_c \approx 90$ K), (2) partially deoxygenated ($T_c \approx 25$ K), 1-mm-long, 60- μm -wide channel, and (3) insulating (semitransparent) transistor borders. Our preliminary measurements indicated a presence of the charging effect in the above structure and showed that in thick YBCO films (~ 200 nm in our case), field-induced modulation of J_c , rather than T_c , is more likely to be observed.¹⁶

The electrical [$R(T)$ and $J_c(T)$] measurements of our test structures were performed in the standard four-probe geometry using a temperature-controlled, computer-driven station. The sample electrical contacts were wire bonded to 300-nm-thick, silver contact pads evaporated directly on top of the oxygen-rich lines. Figure 56.15 shows the $R(T)$ and $J_c(T)$ curves measured for the microbridge presented in Fig. 56.14(a). We note very good superconducting properties of our laser-patterned line. The somewhat unconventional shape of the $R(T)$ dependence is due to the fact that at high temperatures there is a finite contribution from the oxygen-poor YBCO, which is parallel to the microbridge and fills the space [see Fig. 56.14(a)] between the two oxygen-rich contacts. At low temperatures (below 150 K) the resistance decreases linearly since in this temperature range, the resistivity of the oxygen-poor material is very high (see Fig. 56.13). The low-temperature extrapolation of the $R(T)$ curve crosses the resistance axis at the axis origin. The $J_c(T)$ dependence is almost linear, and J_c increases at the rate of about 0.2 MA/cm²/K, reaching above 2 MA/cm² at 77 K.

Figure 56.16 shows in detail the resistive transition presented in Fig. 56.15 (sample W.2-43-A42, open squares), together with the transitions recorded for a laser-written line fabricated on a magnetron-sputtered YBCO-on-SrTiO₃ film (sample UR 168, open squares) and for the corresponding original, as-deposited films (samples W.2-43-A42 and UR 168, closed squares). Comparing the two sets of curves we note that in both cases the laser-patterned lines and the original films exhibit the same ΔT_c and T_{c0} ; thus, a somewhat depressed T_c , observed in the UR 168 sample, should not be associated with the oxygen deficiency but is, apparently, due to the film's non-optimal Y:Ba:Cu cation ratio, or large concentration of defects. The observed differences between the $R(300\text{ K})/R(100\text{ K})$ ratios for the laser-written lines and the original films are due to the finite contribution of the semiconducting YBCO to the actual $R(T)$ —as we mentioned before—explaining the shape of the $R(T)$ presented in Fig. 56.15.

Fig. 56.16

Comparison between the superconducting transitions of oxygen-rich laser-written lines (open squares and open and closed circles) and the original superconducting films (closed squares). UR 168 denotes the 80-nm-thick film deposited on SrTiO₃, while the label W.2-43-A4 corresponds to the 280-nm-thick YBCO-on-LaAlO₃ film. Traces for the laser-written pattern on the W.2-43-A4 film were taken on the same sample right after the laser-patterning process (open squares), as well as two (closed circles) and eight (open circles) months later.

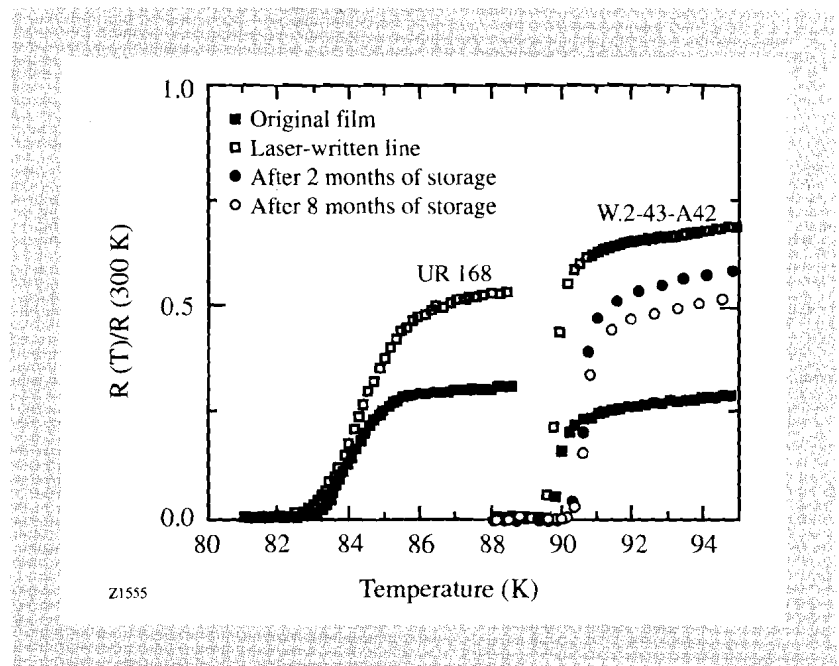


Figure 56.16 also presents two $R(T)$ traces (open and closed circles) measured on the same W.2-43-A42 sample, but two and eight months after the original patterning. During that time our sample was kept at room temperature and exposed to air. We note that instead of expected degradation in the sample's superconducting properties, the laser-written structures actually exhibit slightly enhanced T_{c0} 's and improved $R(100\text{ K})/R(300\text{ K})$ ratios. We associate these effects with a slow process of long-term oxygen ordering, which should lead to the film's "self-improvement." The storage did not lead to any visible changes in the physical appearance of our samples. The superconducting-semiconducting interfaces, as observed under optical and scanning electron microscopes (not shown), remained less than 1 μm wide. The long-term stability of the superconducting and structural properties of our samples demonstrates that, indeed, laser writing is a practical technique for patterning YBCO films.

In conclusion, we have demonstrated that laser patterning can be successfully used to fabricate practical YBCO thin-film devices and circuits. The technique

produces well-defined patterns with undamaged crystalline structure and very sharp (less than 1 μm wide) interfaces. The writing is fully reversible, and the patterns can be either erased by furnace annealing or rewritten by subsequent laser writing. Most importantly, the technique is noninvasive, requires no patterning mask, and results in completely planar, free-of-surface contamination structures. The laser-patterned structures are characterized by superconducting properties, which are as good as those of the original superconducting films, even after many months of shelf storage. We presented a number of completely monolithic test structures that were all fabricated using laser patterning. The devices are intrinsic to the YBCO material (they cannot be reproduced using, e.g., metallic superconductors), and they demonstrate, in our opinion, that laser patterning can be successfully implemented in fabricating a variety of electronic and optoelectronic, high- T_c devices. The technique is especially promising in the YBCO-based optoelectronics since, in this compound, both electrical and optical properties are very sensitive to the sample's oxygen content.

ACKNOWLEDGMENT

The authors would like to thank Professor M. R. Beasley for a very helpful discussion regarding variable-distance hopping. This work was supported by the Air Force Office for Scientific Research grants F49620-92-J-0075 (Rochester) and F49620-91-C-0034 (Westinghouse). Additional support was provided in part by the Polish Government grant 2-04979-I and the Laboratory for Laser Energetics' Frank Horton Graduate Fellowship Program.

REFERENCES

1. See, e.g., A. I. Braginski, in *Superconducting Devices and Their Applications*, edited by H. Koch and H. Lübbig, Springer Proceedings in Physics (Springer-Verlag, Berlin, 1992), Vol. 64, pp. 3–18.
2. P. H. Ballentine, A. M. Kadin, and D. S. Mallory, *IEEE Trans. Magn.* **27**, 997 (1991).
3. See, e.g., P. H. Ballentine, A. M. Kadin, M. A. Fisher, D. S. Mallory, and W. R. Donaldson, *IEEE Trans Magn.* **25**, 950 (1989).
4. M. Rothschild *et al.*, *Appl. Phys. Lett.* **52**, 404 (1988).
5. R. R. Krchnavek *et al.*, *J. Appl. Phys.* **65**, 1802 (1989).
6. R. C. Dye *et al.*, *Appl. Phys. Lett.* **57**, 1149 (1990).
7. Y. Q. Shen, T. Freltoft, and P. Vase, *Appl. Phys. Lett.* **59**, 1365 (1991).
8. R. Sobolewski, W. Xiong, and W. Kula, *IEEE Trans. Appl. Supercond.* **3**, 2986 (1993).
9. R. Sobolewski, in *Superconductivity and Its Applications*, AIP Conference Proceedings 251, New York, NY, 1992, pp. 659–670.
10. J. R. Gavaler *et al.*, *J. Appl. Phys.* **70**, 4383 (1991).
11. See, e.g., D. K. Ferry, *Semiconductors* (Macmillan Publishing Company, New York, 1991). Detailed presentation of the low-temperature hopping transport in oxygen-depleted YBCO thin films will be presented elsewhere.
12. R. Sobolewski, W. Xiong, W. Kula, and B. McIntyre, accepted for presentation during the 20th International Conference on Low-Temperature Physics (LT-20), Eugene, OR, 4–11 August 1993, and to appear in *Physica B* (1993).
13. T. Gong, L. X. Zheng, Y. Kostoulas, W. Xiong, W. Kula, K. B. Ucer,

- R. Sobolewski, and P. M. Fauchet, to appear in *Ultrafast Electronics and Optoelectronics V*, Springer Series in Electronics and Photonics (Springer-Verlag, Berlin, 1993).
14. D. H. Auston, *Appl. Phys. Lett.* **26**, 101 (1975).
 15. R. Sobolewski, W. Xiong, W. Kula, W. N. Maung, and D. P. Butler, submitted for presentation during the 4th International Superconductive Electronics Conference (ISEC '93), Boulder, CO, 11–14 August 1993, and to be published.
 16. W. Kula and R. Sobolewski, accepted for presentation during the 20th International Conference on Low-Temperature Physics (LT-20), Eugene, OR, 4–11 August 1993, and to appear in *Physica B* (1993).

2.B Fabrication of Foam Shells Overcoated with Plastic Layers

Future ICF capsule designs incorporate thick cryogenic layers of fusion fuel (DT). There are a number of techniques currently under investigation to form these thick fuel layers. One such technique is to use a low-density polymer or aerosol (SiO_2) foam matrix to hold the liquid DT. A collaborative effort was undertaken at the Institute for Laser Engineering (ILE) by researchers from both LLE and ILE to explore methods for fabricating polymer foam capsules. These types of capsules, if successful, will be used for experiments to be conducted on the upgraded OMEGA laser system. This report summarizes the knowledge obtained by LLE from this collaborative effort for fabricating foam shell targets overcoated with a plastic layer. Fabrication of the foam shells is described, followed by a description of the process for overcoating the plastic layer on the foam shell.

Fabrication of Foam Shells

The foam shells are fabricated using the microencapsulation technique developed by Kubo¹ and refined by Takagi *et al.*² During this process, the hydrophobic phase consists of a diluted solution of difunctional or multifunctional monomer. After forming shells from this hydrophobic phase, the monomer is polymerized to form a cross-linked polymer gel. The solvent is removed from the gel to obtain a three-dimensional network structure of low-density foam.

In the Osaka experiments, the W_1 , O , and W_2 phases consisted of the composition given in Table 56.II. Fabrication of the foam-shell targets started by mixing 10 g of the O phase and 5 g of the W_1 phase in a 20-ml beaker. The mixture was shaken to form an emulsion of the desired size. The mixture was then poured into a beaker containing 500 ml of the W_2 phase, at a temperature of 45°C, and stirred. The polymerization reaction proceeded for 2 h at 90°C. Upon conclusion

Table 56.II: Composition of the W_1 , O , and W_2 phases.

W_1 phase	0.05% aqueous solution of polyoxymethylene sorbitan monopalmitate
O phase	2%–5% of trimethylol propane trimethacrylate (TMPT), 1:1 mixture of diethyl phthalate and di-n-butyl phthalate, 2, 2' izobis-isobutyronitrile (AIBN) as a polymerization initiator (10% of TMPT), and 0.1%–0.5% of sorbitan monopalmitate
W_2 phase	5%–12.5% of PVA solution in water (DP of PVA: 500)

of the reaction, the O phase had completely gelled. The whole system was washed gently with water several times, and the shells were gently introduced into a beaker containing 100 ml of toluene. The water separated to the bottom of the beaker and was removed using a pipette. The shells settled to the bottom and about 2/3 of the toluene was decanted; 1,2 dichloroethane was then added. Solid spheres and the broken shells sank to the bottom, and the good shells floated on top since they are buoyant in 1,2 dichloroethane due to the encapsulated water. The good shells were collected in ethanol using a pipette, and the ethanol replaced the water inside the shells.

The foam shells were characterized while they were both immersed in ethanol and in a dry state. (A few of the shells in ethanol were dried using a CO_2 critical-point drying method.) Figure 56.17 shows a microscopic image of a foam shell in ethanol. The foam wall thickness is 120 μm , and the concentricity is very good. The outer diameter of the shell is 800 μm . A typical batch contains shells having a wide range of sizes and wall thicknesses that encompass the range of interest for OMEGA Upgrade experiments. In general, the wall thickness depends more on the concentration of PVA in the W_2 phase, and less on the concentration of TMPT in the O phase. Figure 56.18 shows the effect of the PVA concentration on the wall thickness. Since any given batch of foam shells contains shells with a wide range of sizes and wall thicknesses, Fig. 56.18 should be interpreted qualitatively. The cell structure of the foam is shown in Fig. 56.19. The cell size ranges from less than one to a few microns. It is not known at present what controls the cell size. Different compositions of the O phase may give different cell sizes and structures; the effect of this composition will be studied later. Figure 56.20 shows the surface structure of a dried foam shell. The density of the surface appears greater than that of the bulk of the foam, possibly due to an interfacial effect between the O phase and the W_2 phase. That is, the chain conformation of the polymerized TMPT at the interface may not be Gaussian, as it is in the bulk, particularly in the direction perpendicular to the interface. As a result, the density of the chains at the interface becomes higher than that inside the bulk. The density of the foam shells was determined by measuring the weight of each shell with a microbalance and measuring their corresponding diameter and wall thickness. The density of ten shells was measured and its mean was calculated. The shells were from a batch made using a 3% TMPT solution and a 2.5% PVA solution. The average foam density was 57.9 mg/cm^3 with a standard deviation of 5.0 mg/cm^3 . The density measured is generally higher than that calculated from the concentration of TMPT. This discrepancy is considered to arise from the contraction of the shell during the drying process.

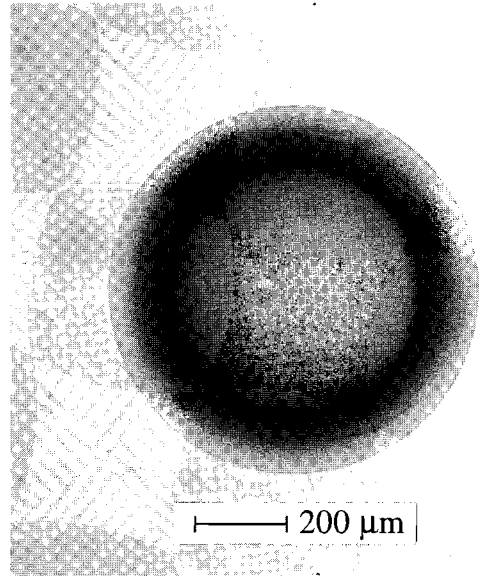
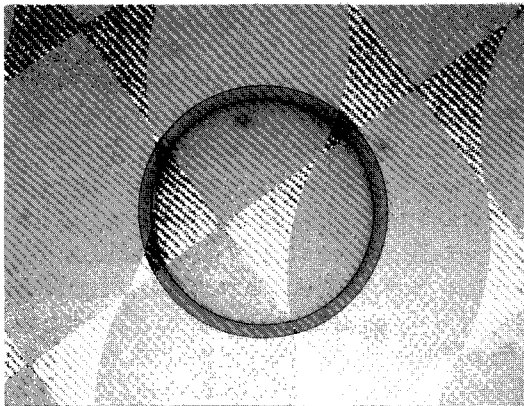


Fig. 56.17
Optical micrograph of a foam shell immersed in ethanol.

T1170



T1126

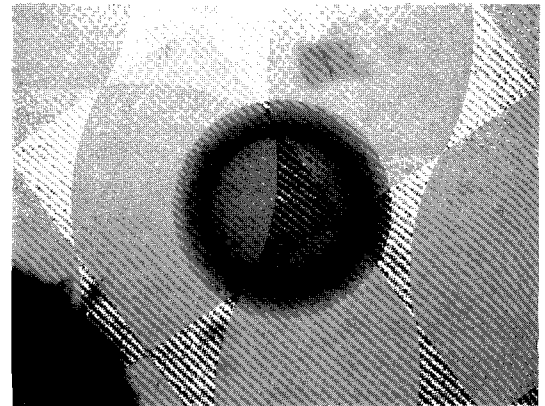
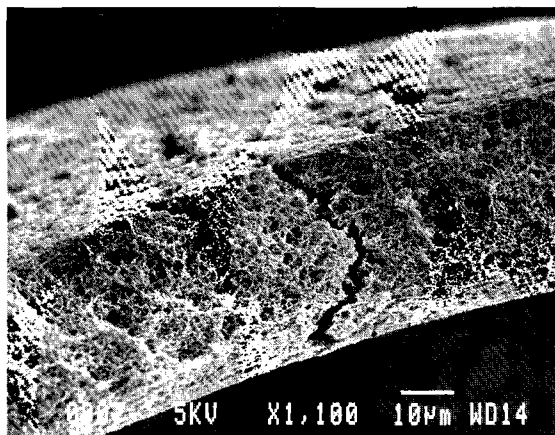


Fig. 56.18
Effect of PVA concentration in the W_2 phase on the wall thickness of foam shells.



T1128

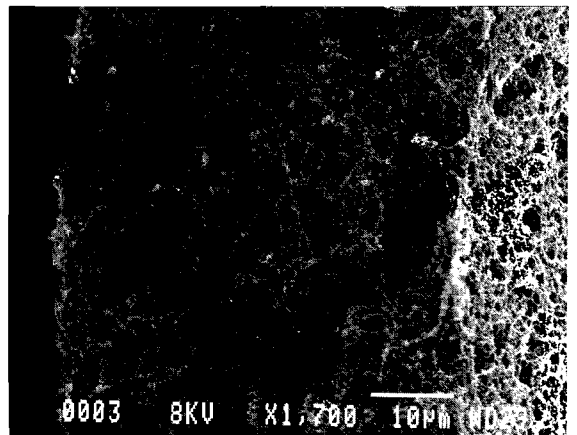


Fig. 56.19
SEM photos of a fracture cross-section of a foam shell.

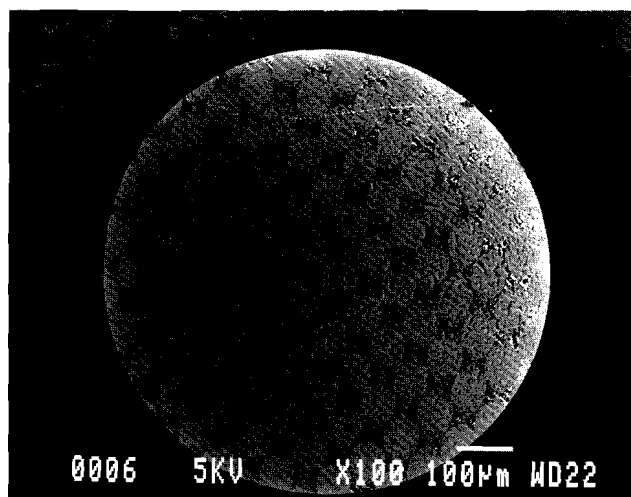


Fig. 56.20
SEM photo of the outer surface of a dried foam shell.

T1127

Fabrication of Plastic-Layer-Overcoated Foam Shells

Overcoating foam shells with a plastic layer is performed by the interfacial polycondensation method.³ In this method, two reagents dissolved in separate phases that are immiscible in each other react to form a condensed polymer layer that is not soluble in either phase. In the experiments performed at Osaka, hydroxy ethyl cellulose in the W_2 phase and isophthaloyl chloride in the O phase react at the interface of the O phase and the W_2 phase (the outer surface of the foam shell) to form cross-linked hydroxy ethyl cellulose. This method, combined with the microencapsulation technology, produced a polymer layer overcoating on the foam shells.

Figure 56.21 is a schematic showing the polycondensation interfacial polymerization process. Foam shells are impregnated with an oil-soluble reagent, which is dispersed in the matrix of an aqueous solution of another reagent. The two reagents react on the interface to form a cross-linked polymer layer on the foam shells. The foam shells are then collected and dried using a CO_2 critical-point drying method. For this reaction, the shells and the reagents are prepared in the following way. First, the foam shells fabricated previously and stored in ethanol are transferred into *p*-chlorotoluene. A complete replacement of ethanol by *p*-chlorotoluene is necessary, and during the replacement process, care must be taken not to damage the fragile shells. The shells are then transferred into an isophthaloyl chloride solution in *p*-chlorotoluene (concentration of 1 mmol/ml) and kept in this solution long enough to ensure saturation. By mixing this with a PVA solution, the excess *p*-chlorotoluene solution is stripped off leaving only saturated foam shells. The foam shells in the PVA solution are poured into a 2-wt% aqueous solution of hydroxyl ethyl cellulose containing 0.5 wt% of polyoxymethylene sorbitan monopalmitate as a surfactant. The polycondensation reaction does not start until the addition of Na_2CO_3 . Since the reaction is reversible, the resulting HCl must be removed to stabilize the reaction. The rate of formation of the plastic layer overcoating was relatively fast, yielding a 7.5- μm layer within 45 min. This reaction forms a flaky surface, which is smoothed by adding NaOH. The whole system is then neutralized by the addition of diluted HCl. The resulting shells are thoroughly washed with water, stored in dioxane, and then dried using the CO_2 critical-point drying apparatus.

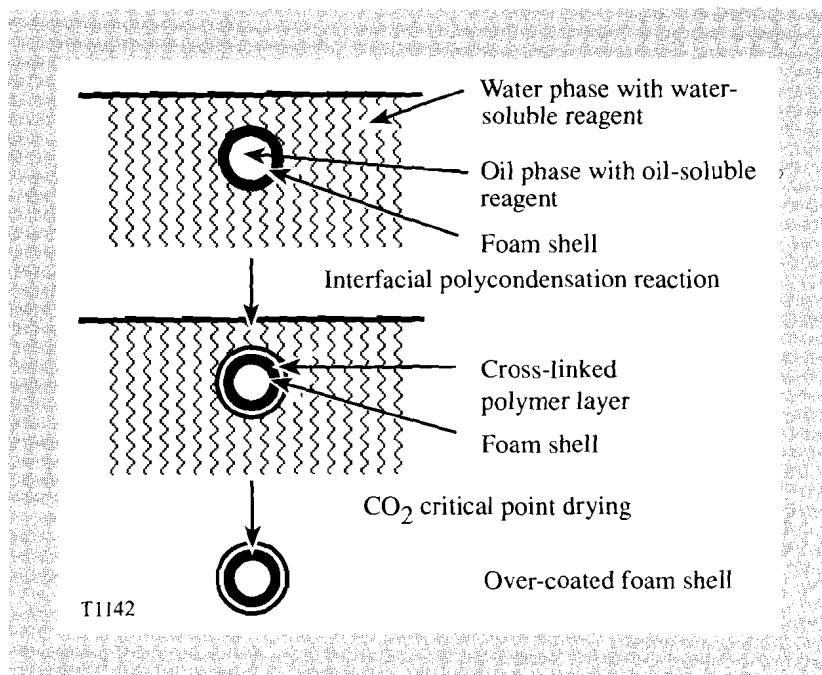


Fig. 56.21
Schematic diagram showing the polycondensation interfacial polymerization process.

Figure 56.22 shows an optical micrograph of the plastic-layer-overcoated foam shell in water. The thickness of the layer can be easily controlled by adjusting the reaction time. A cross-section of the plastic-layer-overcoated foam shell in Fig. 56.23 shows that the adhesion of the plastic layer to the outer surface of the foam shell does not replicate the foam structure, but forms a clean spherical surface. This may be due to the fact that, during the polycondensation reaction process, the interface between the *p*-chlorotoluene-containing shells and the hydroxyl-ethyl-cellulose-containing matrix was always spherical. A scanning electron microscope (SEM) photo in Fig. 56.24 shows that the surface of the plastic overcoating is smooth and void of defects. Furthermore, as previously described, any defects on the surface can be removed by hydrolysis using NaOH.

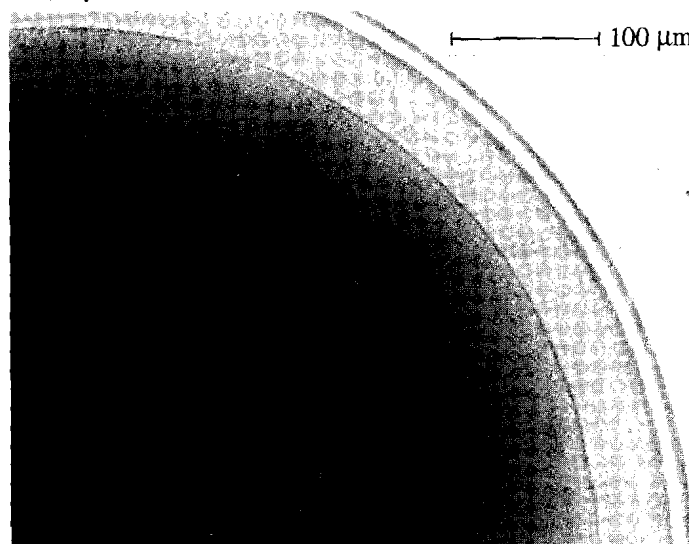
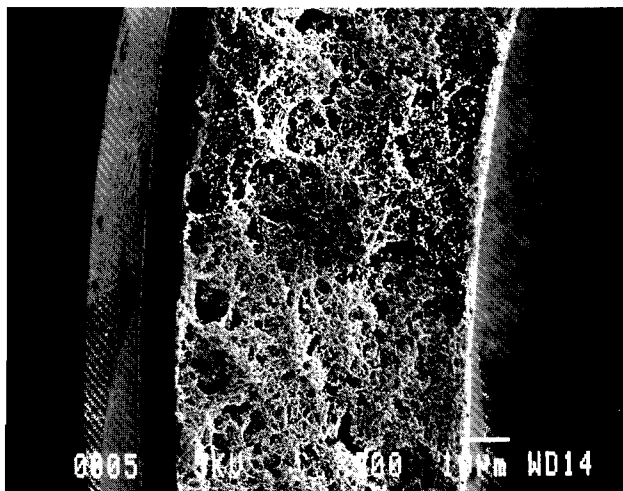


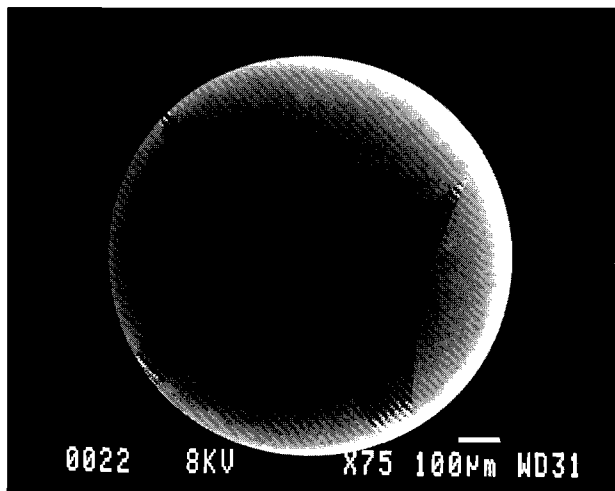
Fig. 56.22
Optical micrograph of a plastic-layer-overcoated foam shell in water.



T1136

Fig. 56.23

SEM photo showing a cross-section of a plastic-layer-overcoated foam shell.



T1135

Fig. 56.24

SEM photo of the surface of a plastic overcoating on a foam shell.

Experience at Osaka University's Institute of Laser Engineering indicates that foam shells with the specifications needed for OMEGA Upgrade experiments can be fabricated using the microencapsulation technique developed at Osaka. It is possible to fabricate plastic-layer-overcoated foam shells having diameters of 0.5–1.5 mm, foam shell thicknesses of 10–120 μm , sphericity and uniformity better than 98%, a foam density of $\sim 50 \text{ mg/cm}^3$, an overcoated-plastic-layer thickness of 3–12 μm , and a plastic layer with an rms surface roughness less than 0.1 μm . The foam density and cell size may be controlled by the proper choice of the chemical composition of the *O* phase during the microencapsulation process. This work remains to be done.

ACKNOWLEDGMENT

It is a great pleasure to acknowledge the hospitality extended to the author during his stay in Japan by Osaka University's Institute of Laser Engineering. He expresses his particular gratitude to Mr. Takagi and Dr. Norimatsu for their assistance and guidance during the course of this work.

REFERENCES

1. U. Kubo and H. Tsubakihara, *J. Vac. Sci. Technol.* **A4**, 1134 (1986).
2. M. Takagi, T. Norimatsu, T. Yamanaka, and S. Nakai, *J. Vac. Sci. Technol.* **A(9) 4**, 2145 (1991).
3. E. L. Wittbecker and P. W. Morgan, *J. Polym. Sci.* **60**, 289 (1959).

Section 3

NATIONAL LASER USERS FACILITY NEWS

The NLUF Steering Committee has received six proposals to evaluate for FY94. The proposals include experiments on GDL plus diagnostic-development projects for the OMEGA Upgrade. A brief summary of each proposal follows:

Proposal 180

“Measurements of Quantum Electrodynamically-Sensitive Transitions in Na-like and Cu-like Ions”

Principal Investigator: **J. Reader**, National Institute of Standards and Technology (NIST)

The principal investigator proposes using GDL to measure QED effects in high-Z ions. There are 11 proposed targets ranging in Z from 47 to 92. The GDL laser system will be used to study Na-like and Cu-like ions of these elements. The primary diagnostic is a 2.2-m Rowland Spectrograph (owned by NIST) with an attached target chamber. The optical system that is intrinsic to the spectrograph is incompatible with the beam geometry of the GDL system. Optics available from the LLE inventory can overcome this incompatibility with the focus lens requiring adaption to the spectrograph's target chamber.

Proposal 181

“Normal-Incidence Multilayer Mirror X-Ray Microscope”

Principal Investigator: **J. F. Seely**, Naval Research Laboratory (NRL)

This NRL group plans to build a Cassegrain-type microscope for use at a 33.7-Å wavelength. The work builds upon the successful fielding of a similar instrument on the OMEGA laser system in 1992 and development work supported by NASA. The proposed microscope will have a 1.8-μm resolution at the target and a magnification of 10 and will use a 1024 × 1024 CCD as the detector. Most of the work will be done at NRL, and the microscope could be tested on either GDL or NOVA. The main concern about this proposal is whether the 33.7-Å wavelength is too long to give useful information about the target's

status during the implosion. The answer is not obvious when shaped laser pulses are used for the implosion.

Proposal 182

“Temperature-Dependent Tensile Strength, Surface Roughness Diagnostics, and Magnetic Support and Positioning of Polymer ICF Shells at Temperatures between 4 K and 300 K”

Principal Investigator: **A. Honig**, Syracuse University

This proposal includes three independent tasks to be done at Syracuse University. The first task is to study the material properties of CH shells at cryogenic temperatures; the second task uses the measured shell properties with precharacterized shells to determine if there is a correlation between accommodation coefficients and surface roughness; and the third task will develop the use of ferrite-doped plastic shells for magnetic levitation and positioning. This work uses much of the technology for handling cryogenic targets developed by the principal investigator over the last four years.

Proposal 183

“The Ion-Acoustic Decay Instability in a Large-Scale, Hot Plasma Relevant to Direct-Drive Laser Fusion—Applications to a Critical Surface Diagnostic and Thermal Smoothing”

Principal Investigator: **K. Mizuno**, Plasma Physics Research Institute (UCD)

This group has proposed a study of the critical surface using the ion-acoustic decay instability. The development of this diagnostic for the OMEGA Upgrade is to be undertaken first with subsequent testing of thermal-smoothing techniques on GDL. A second task will use the GDL facility to test the second-harmonic diagnostic and will use x rays emitted from flat targets to study thermal smoothing and lateral heat transport. This second task requires that GDL have full pulse-shaping and smoothing-by-spectral-dispersion capability. In addition, there is the need for a large-aperture polarizer to modify the high-intensity portion of the laser pulse.

Proposal 184

“Plasma Spectroscopy: Theoretical and Experimental Diagnostic Development/Tests”

Principal Investigator: **C. F. Hooper, Jr.**, University of Florida

The principal investigator proposes to continue the development of atomic physics computer codes to calculate the effects of high temperature and density on x-ray line emission and transport. There are three tasks associated with this work: The analysis of *L*-shell spectra is considered (by the principal investigator) the next step in the extension of the atomic models with ion dynamics formalism. It is also proposed to extend the “multielectron-line-broadening theory” to conditions expected for OMEGA Upgrade target implosions. The third task is unrelated to the above efforts and proposes to develop micro-dot spectroscopy to study laser-plasma interactions.

Proposal 185

“Development of Density and Temperature Profile Diagnostics for ICF Targets”

Principal Investigator: **H. R. Griem**, University of Maryland

The work proposed is to extend the development of previous work in x-ray and XUV spectroscopy to the OMEGA Upgrade. The diagnostics must be constructed and tested before the experiments can be done on the OMEGA Upgrade; in the meantime GDL will be used to continue this development.

Section 4

LASER SYSTEM REPORT

4.A GDL Facility Report

Refurbishment of GDL continued during the fourth quarter of FY93. Activity concentrated on the installation of an imaging system to aid system alignment and the assembly of the second driver line that generates the so-called "foot" pulse.

The imaging system can acquire data from selected outputs of 17 video cameras located throughout the system, to one of five monitor pairs strategically located in the laser bay. The cameras view beamline centering and/or pointing at the ends of the various "legs" of the system. Dual monitors permit the operator to view simultaneously both centering and pointing images for a beam. Software-settable cross-hair references, beam cross-hair finding, and centroid-finding routines that operate at the 5-Hz repetition rate of the regenerative amplifiers are available. The imaging-system platform consists of a pair of 33-MHz 486 PC's that each contain two video frame grabbers and three LLE-designed-and-built, 5:1 (or 1:5) video multiplexers. Camera horizontal and vertical sync signals and frame-grabber trigger signals are derived from the laser's timing system to ensure proper synchronization of the image capture. Hand-held terminals located near the monitor pairs permit selection of the camera(s) to be viewed as well as selection of software routines. This system, along with new alignment sensor packages scheduled for installation in the first quarter of FY94, has and will ease alignment of the GDL system.

Significant progress was made in the installation, activation, and characterization of the foot-pulse driver line. This second driver line produces

the central beam of the co-propagated beam shape, which will also be used in the OMEGA Upgrade. The driver consists of a fiber-fed regenerative amplifier and a large-aperture ring amplifier (LARA). The system was activated in September. An energy and beam phase characterization was completed by the end of September and will be reported on in a future LLE Review article.

Simultaneous with the foot-driver-line activation, an annular apodizer was installed into the existing main-pulse driver line. Testing with this apodizer successfully produced the annular-shaped beam required for the main pulse. The outputs of the foot-pulse and main-pulse driver lines were merged on a beam combiner (a 45°-angle-of-incidence mirror with a central hole) to produce the first successful co-propagated beam. Work will continue in GDL during the first quarter of FY94 to propagate this beam shape through the system.

Finally, construction of the output end of the system continued during the fourth quarter. The system-output spatial filter was assembled, put under vacuum, and collimated. This spatial filter magnifies the clear aperture from 20 cm to 28 cm just prior to frequency conversion.

ACKNOWLEDGMENT

This work was supported by the U.S. Department of Energy Office of Inertial Confinement Fusion under Cooperative Agreement No. DE-FC03-92SF19460, the University of Rochester, and the New York State Energy Research and Development Authority. The support of DOE does not constitute an endorsement by DOE of the views expressed in this article.

4.B OMEGA Upgrade Status Report

Construction on the laser bay and target bay was completed by the end of August 1993, precisely on schedule. After taking occupancy of the building, LLE staff and contractors began the integration phase, which saw the first of the major structures entering the building for cleaning, alignment, and grouting into their exact final location on the laser bay floor. The stage-F alignment sensor package (FASP) structures, which are massive (30-ton) castings composed of a crushed granite and epoxy composite, have been placed in the target bay for imminent positioning and grouting.

The OMEGA Upgrade design is complete, as of 30 September 1993, and the final review documentation has been submitted to DOE. An Executive Summary has been provided, which contains a detailed overview of the complete system design. This issue of the LLE Review provides an excerpt from the Executive Summary, Sec. 5, which provides overviews of all of the major subsystems. Due to the length of this document, this issue will include subsystems from Laser Drivers through Amplifier Subsystems. Subsequent issues will include the remaining subsystem descriptions, such as Power Conditioning, Controls, Optomechanical Design and Major Structures.

Laser Drivers

1. Oscillators

The OMEGA Upgrade laser drivers comprise six synchronized oscillators: one continuous-wave (cw) mode-locked master oscillator; four regenerative amplifiers (regens); and one single-axial-mode (monomode), long-pulse oscillator. Extensive diagnosis and synchronous timing of these oscillators ensure the delivery of pulses with proper duration, precisely timed with respect to one another.

All oscillators and regens use crystals of Nd-doped yttrium lithium fluoride (Nd:YLF) as the active medium. The wavelength of this material matches well that of the phosphate glass amplifiers, and its material constants, particularly its gain and thermal properties, are ideally suited for oscillator applications. All oscillators and regens operate in a single transverse electromagnetic mode (TEM_{00}).

The master oscillator is a commercial cw mode-locked oscillator. This unit is a highly stabilized, actively mode-locked oscillator delivering a train of pulses of 80-ps duration at a rate of ~76 MHz. This oscillator operates in a thermally controlled environment and is extensively diagnosed to ensure stability. These diagnostics are discussed later in this article. The master oscillator provides the seed optical pulse to three regens: the main-, foot-, and short-pulse oscillators. Coupling between these oscillators is accomplished using optical fibers, ensuring flexibility and alignment insensitivity. In addition to providing the seed pulses (which define the timing of the shot event), the rf signal driving the mode locker is used as a reference for the electrical timing system. This timing system provides rates and timing fiducials for the portions of the laser system requiring timing to no better than 0.5 ns. Timing of events requiring higher precision (i.e., <0.5 ns) will be timed to this laser pulse using photodetectors. Triggering optical switches with the laser pulse provides a means to absolutely time events to the shot.

The need to frequency convert the OMEGA Upgrade laser to its third harmonic imposes the stringent requirement that each regen oscillator should operate with the same central wavelength. This need arises because each pulse (main and foot) will ultimately be frequency tripled by the same crystal and will require similar divergence, alignment, and wavelength. It is therefore necessary to monitor, control, and maintain a predetermined central wavelength for both oscillators. To limit the loss of main-pulse conversion efficiency to 0.5% the acceptable mismatch in wavelengths is ~0.2 Å. However, the implementation of SSD will require measurement of the central wavelength to <0.2 Å because spectral dispersion transforms frequency shifts to pointing shifts. To provide better wavelength stability the regens are fitted with temperature-stabilized etalons.

2. Regenerative Amplifiers

The first amplifiers for the main, foot, and short pulses are regens,¹⁻³ deriving their seed pulse from the master oscillator as indicated in Fig. 56.25. A single-mode, polarization-preserving optical fiber provides the link between the master oscillator and these regens. The regen cavity is a stable resonator operating in the

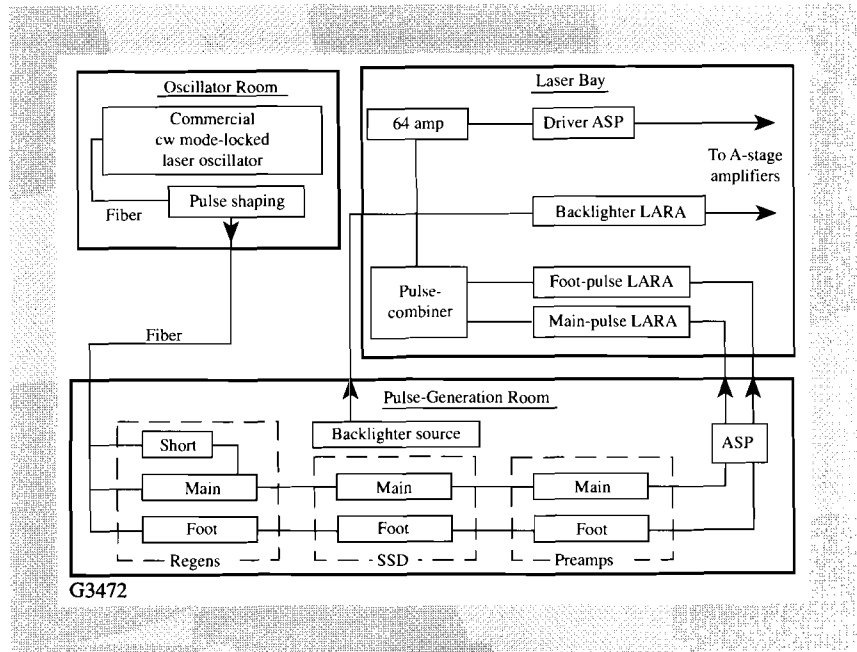


Fig. 56.25
A block diagram of the laser-driver subsystem, which comprises three separate areas: oscillator room, pulse-generation room, and the laser-bay driver line.

TEM₀₀ mode (Fig. 56.26). The duration of the pulses emitted by each regen depends on the intra-cavity etalons that temporally stretch the pulse as it circulates in the cavity. The short-pulse regen produces a pulse that can trigger electro-optical switches for truncation and pulse shaping. This requires <100-ps pulses, which are produced using no etalon in the cavity. The performance requirements for these regens are shown in Table 56.III.

Fig. 56.26
The main-pulse regen is coupled (via an optical fiber) to the master oscillator. A similar configuration for the foot pulse ensures precise timing between the two pulses.

For other future applications requiring pulses synchronized to the main laser pulse, it is possible to add more regens seeded by the master oscillator. This is planned for any optical probe beams that will be needed. These regens will be housed in areas remote from the laser driver rooms.

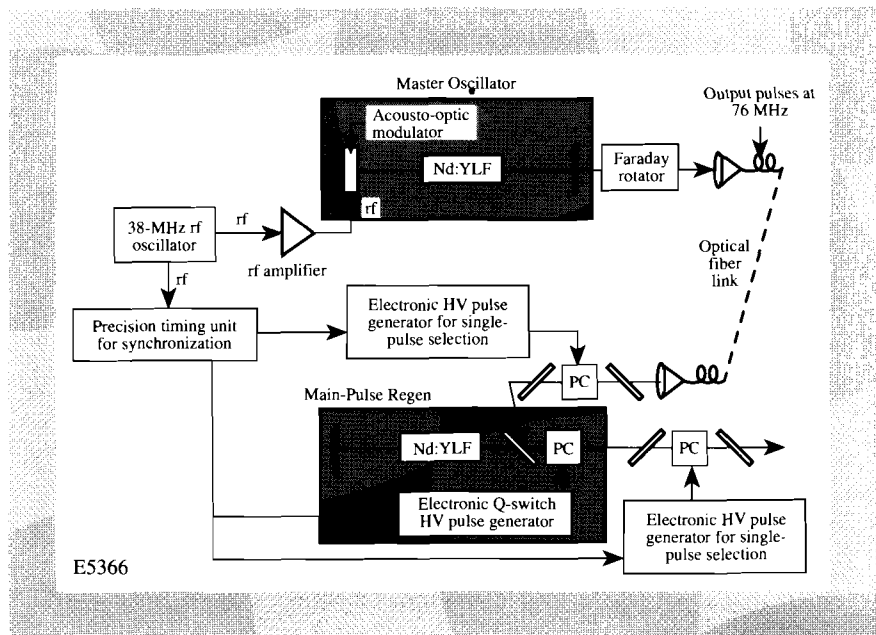
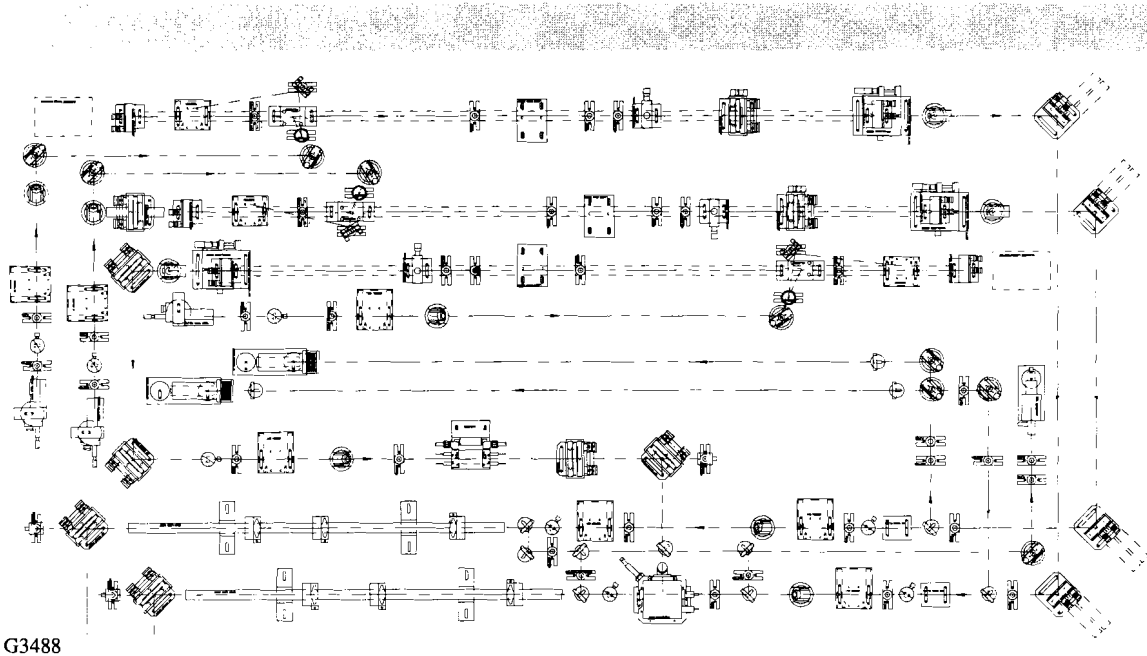


Table 56.III: Performance requirements of principal oscillators.

	Main-Pulse Oscillator	Foot-Pulse Oscillator	Short-Pulse ^(a) Oscillator
Seed pulse	cw mode-locked master oscillator		
Oscillator type	regen	regen	regen
Output energy (single pulse)	~1 mJ	~1 mJ	~1 mJ
Amplitude stability	≤2%	≤2%	≤2%
Pulse duration	0.5–1 ns	5–20 ns	0.1–1 ns
Temporal jitter between foot and main pulse	<30 ps	≤30 ps	≤30 ps
Pointing stability	≤10 μrad	≤10 μrad	≤10 μrad
Energy contrast (inter-pulse contrast)	>100,000:1	>100,000:1	>100,000:1
(a) This third regen is used for synchronized optoelectronic pulse shaping.			

A fourth regen is used to amplify the backlighter pulse. This regen obtains its seed pulse from a long-pulse oscillator rather than from the master oscillator. The backlighter laser driver is discussed later. The use of a single (instead of multiple) master oscillator for all three oscillators was chosen to simplify synchronization of the many pulses generated. A layout of the regen table, which contains all of these oscillators, is shown in Fig. 56.27.

Fig 56.27
The regen table, in the pulse-generation room, has three (main-, foot-, and short-pulse) regens on it.



Reliable performance of regens requires high-contrast seeding, i.e., injection into the regen of a single pulse with high contrast. This is necessary since, in general, the cavity lengths of the master oscillator and the regens are not identical, and experience has shown that this leads to inter-pulse noise in the output pulse train from the regens. High contrast of the seed pulse is provided by an injection-isolation Pockels cell for each regen.

Synchronization of the master oscillator and the regen is provided by the pulse injected into the regen; the regen acts essentially as an optical delay line. However, the single-pulse switch-out in the injection path, the Q-switch in the regen, and the Pockels cell used for single-pulse selection following the regen must all be rigorously timed (phased) to the 38-MHz rf signal driving the acousto-optic mode-locker in the master oscillator. This is accomplished by the precision timing system mentioned later.

Amplitude stability of the single pulse selected for amplification in the main-pulse driver line is essential. This requires Q-switching of the regen under conditions of controllable and repeatable gain (population inversion) in the active medium. These conditions can be obtained from cw, quasi-cw, or pulsed operation of the Nd:YLF gain medium with adequate diagnosis. Further stabilization is achieved by using the intracavity intensity as feedback for control of the cavity losses. This control is implemented by the cavity Q-switch electronics.

3. Backlighter Source

In anticipation of x-ray backlighting experiments requiring a different type of laser pulse, provisions have been made to inject a third laser driver into 20 beamlines of the OMEGA Upgrade system. The source for this pulse consists of a single-axial-mode (monomode), long-pulse oscillator that seeds a regen similar to the others described earlier. This monomode oscillator produces a 20-ns pulse that is electro-optically chopped and then amplified by a regen. Synchronization of the self-injection-seeded monomode laser is accomplished through the timing of the cavity Q-switch and the electro-optic switch.

4. Synchronization of Oscillators and the Timing System

The requirement for synchronization of the various oscillators and electro-optical components is ≤ 30 ps. This is easily achieved because a single pulse is used to seed all of the regenerative amplifiers. The timing of the various electro-optical devices and electronic diagnostics is provided by the master timing system—a multicircuit system that generates both the rates and synchronization for the system. A block diagram of this system is shown in Fig. 56.28.

The master timing assembly is part of the laser drivers subsystem and will be located in the pulse-generation room. This unit will accept a master timing signal (nominally 38 MHz) from the master oscillator (optical) in the oscillator room. The rf mode-locked driver for this laser serves as the optical master oscillator for the OMEGA Upgrade. It will also accept two separate, hard-wired asynchronous “enable” signals from the power-conditioning host workstation and will be connected to an “inhibit loop” that links to other hardware and software devices.

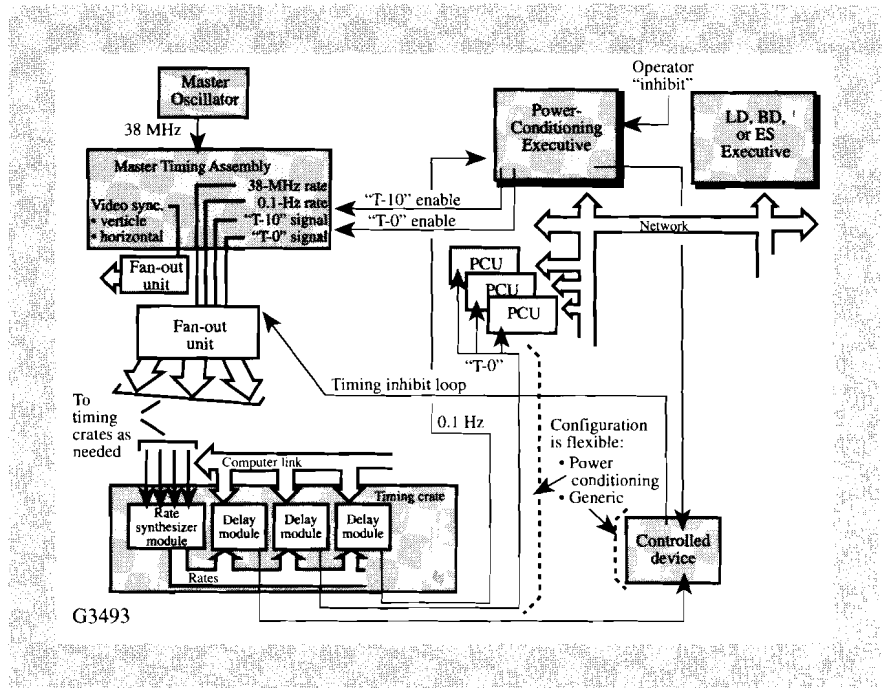


Fig. 56.28
 The timing system is referenced to the 38-MHz rf signal that drives the master laser oscillator. Various slower rates are generated and distributed by this system.

The master timing assembly will output synchronized periodic timing signals and synchronized copies of the power-conditioning “enable” signals to associated “fan-out” boxes. The fan-out boxes will feed signals to the modular timing units. Fan-out boxes for video-synchronization, 38-MHz, and logic-level outputs are planned. The “inhibit loop” signal will be capable of interrupting all of these outputs.

The modular timing units will be located near the equipment they control and will provide a precisely delayed synchronous output signal of the appropriate voltage and duration. The synchronization rate source will be software selectable and will be based on the master timing assembly outputs. The output signal will be delayed relative to the input signal by a programmable value.

5. Smoothing by Spectral Dispersion (SSD)

Accommodations have been made for the implementation of SSD⁴ in the laser driver. During the design of the PGR, the beam size and the optical layout were chosen to allow for the installation of the pre-delay gratings and the electro-optic modulator. In the laser-bay driver line, image planes were provided in the foot- and main-pulse optical systems to accommodate the placement of the angular dispersion gratings. Calculations were performed to determine the location of these gratings and the effect that their insertion will have on the placement of other optical components, namely alignment fiducials. To compensate for the insertion losses of the SSD components, preamplifiers have been added to the foot and main pulses.

6. Preamplifiers

The preamplifiers are small rod amplifiers that use conventional technology and are designed to operate at high repetition rates. The rods are high-quality ($\lambda/10$ @ 633 nm), 7-mm-diam Nd:YLF laser glass. The pump modules and

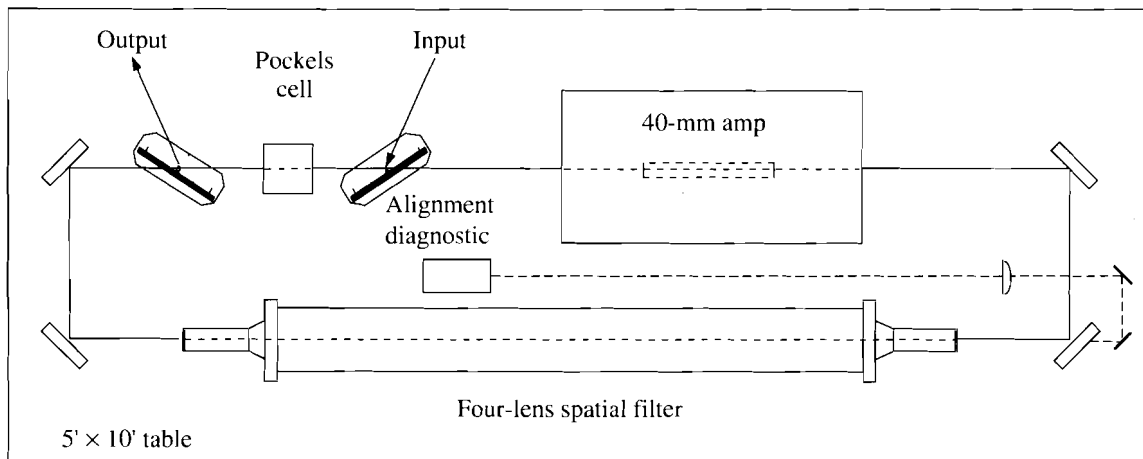
power conditioning are commercially available components. These amplifiers will be capable of operating at ~ 1 Hz with gains of ≥ 50 . When used with the regenerative amplifiers, the output pulses will be of sufficient energy to facilitate real-time alignment and maintenance of the laser system.

7. Large-Aperture Ring Amplifier (LARA)

In traditional laser-driver configurations the final portion of the system staging is comprised of single-pass amplifiers; the number required is determined by the desired gain and output energy. By contrast, the Upgrade utilizes a single LARA for compactness and simplicity. This amplifier provides high gain ($>20,000$) and repeatable high-quality beams for pulses in the 0.1- to 10.0-ns range.

The LARA is a type of regenerative amplifier that uses a relatively large (40-mm) rod amplifier, a spatial filter, and an optical switch, all contained in an optical ring. Pulses are injected into the ring, circulate 3–4 round trips, and are switched out. During each round trip the pulse encounters an amplifier gain of about 14. This gain value is relatively conservative since a 40-mm amplifier can provide gains of 15–20 in this regime. This conservatism helps improve the reliability of the amplifier and provides ample reserve gain for future needs.

A schematic of the optical layout for the LARA is shown in Fig. 56.29. Central to its performance is the four-lens spatial filter that provides image relaying such that any location within the ring is mapped onto itself on subsequent round trips. This feature affords the ability to accurately align the ring and ensure that the optical path is reproducible, thereby allowing control of beam quality at high gain. The round-trip path length is approximately four times the effective focal length of each lens pair.



E6591

Fig. 56.29

The large-aperture ring amplifier (LARA) used in the OMEGA Upgrade laser driver. The Pockels cell admits the input pulse and then, after four round trips, switches the amplified pulse out. The four-lens spatial filter is used in defining the alignment axis.

The spatial filter pinhole is mounted to a pre-aligned position that serves as a pointing reference for alignment of the ring. The mount is kinematic so that the pinhole can be removed during fine alignment of cross hairs and accurately placed. The internal alignment of the LARA can be precisely maintained by aligning an intra-ring cross hair to itself and by aligning the beam to the spatial-filter pinhole using mirrors within the ring. An external beam is then injected into the ring and aligned to these references using external mirrors.

The injection and rejection (input and output) of pulses is performed using a Pockels cell and two polarizing beam splitters. Switching of the Pockels cell is driven by a thyatron-based switching circuit feeding a charge line; a switching time of much less than the cavity round trip time (22 ns) is achieved. The system will use a 66-ns charge line to provide four passes through the amplifier. The output prepulse contrast is better than 1000:1 and when followed by an isolation cell, a LARA can easily exceed the $10^5:1$ contrast requirement.

The gain performance of the LARA versus the capacitor bank energy is shown in Fig. 56.30. Total gains of greater than 40,000 have been obtained with no appreciable degradation in beam quality (see Fig. 56.31). The design and performance of the LARA is presented in Ref. 5.

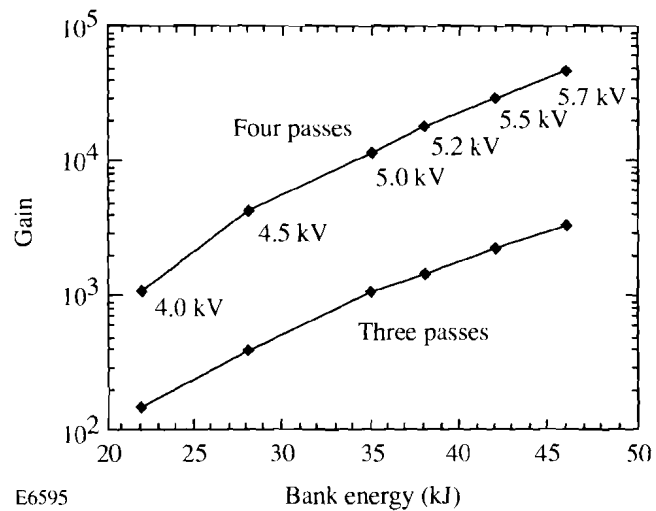


Fig. 56.30

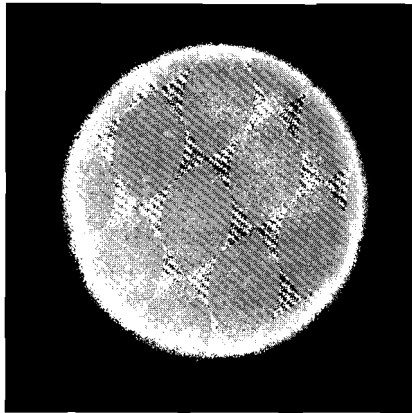
The total gain of the LARA system as a function of capacitor bank energy. Gains greater than 10,000 are easily achieved with four passes through the ring.

8. Laser Driver Diagnostics

The propagated beam characteristics measured by the laser driver diagnostics can be divided into four categories:

- (a) Energy
- (b) Single-pulse and pulse-train-envelope FWHM
- (c) Pockel cell timing jitter
- (d) Spectral bandwidth and central wavelength through SSD

A laser driver's executive workstation host will collect data from these single-beamline diagnostics using the following measurement systems:



E6596

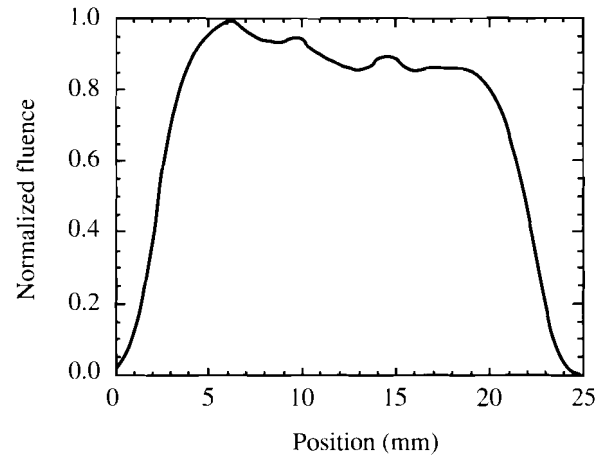


Fig. 56.31

The LARA output-beam image (and a lineup through it) for a 1-ns pulse with four round trips. The asymmetry in the intensity was caused by a misalignment of the input beam rather than by the performance of the LARA.

- Master oscillator monitoring and stabilization
- Regenerative amplifier (regen) characterization
- SSD (smoothing by spectral dispersion), laser-bandwidth broadening
- LARA characterization.

a. Laser-energy measurements. Energy measurements are made at several points along the laser drivers using photo-diodes that have been calibrated with a calorimeter. The charge created in each photodiode by the optical signal is integrated. The energy measurements are made at the 5-Hz cycle rate of the system, and real-time running statistics are computed from this data stream.

b. Single-pulse and pulse-train-envelope widths. The full width at half-maximum (FWHM) of both the single pulse and the cavity pulse-train envelopes are made at several key points within the system. The relatively slower, ~2-ms FWHM, pulse-train envelopes are sampled by standard photodiodes. The output signals are low-pass frequency filtered and captured by ~200-MHz digitizing oscilloscopes. These waveforms are read out of the oscilloscopes through their general-purpose-interface-bus (GPIB) communication ports, and the data are uploaded to the main diagnostic control computer for analysis. The much faster, ~1-ns FWHM, single pulses are sampled by fast vacuum photodiodes and high-bandwidth, ~5.0-GHz, transient digitizing oscilloscopes. In both cases, optimized communications and reduction software is used to meet the 5-Hz cycle rate of the laser system. Real-time running statistics are computed from this data stream and used to monitor the operational status of the system.

c. Pockels cell timing jitter. Pockels cells are used throughout the laser drivers to facilitate the operation of the system. The variation in the time delay between the origination of the Pockels cell trigger signal and the time when the full electric field appears across the cell is a key parameter that affects the pulse-to-pulse uniformity of the laser driver output. These timing variations, called "jitter," are of the order of ~1-ns high speed, 50 ps per count; time-to-digital converters

(TDC's) are used to make these jitter measurements. The TDC's use separate electrical input triggers to start and stop the internal counters. The start-counting trigger is derived from the master-timing fan-out, and the stop-counting trigger is generated by the electronics that drive the electric field on the Pockels cell. The number of counts within the TDC is read out, and the data are uploaded to the host computer for analysis. Real-time running statistics are computed from this data stream and used to monitor the operational status of the system.

d. Spectral bandwidth and central wavelength from SSD. The spatial intensity and phase uniformity of the laser beam are enhanced by using a technique based on SSD. This process is implemented within the laser drivers. The correct central wavelength and amount of bandwidth broadening of the laser after the SSD are important for high-efficiency, third-harmonic conversion. To monitor these parameters, spectral measurements are made to an accuracy of $\pm 0.02 \text{ \AA}$ using a high-dispersion spectrometer. The detector coupled to the spectrometer output is a slow-scan, cryogenically cooled CCD array with 18 bits of dynamic range. The low quantum efficiency of the detector at 1 \mu m is overcome by efficiently coupling the light into the spectrometer (i.e., matching numerical apertures) and by sampling a high percentage (4%) of the laser-beam energy. The output of the array is buffered by an intermediate local controller and then passed along to the high-level diagnostic computer. This system is designed to operate at 1 Hz, collecting data on every fifth cycle of the laser. The spectrum of the pulse that is propagated for a full-system, high-power shot is always collected, independent of the 1-Hz acquisition rate. Real-time running statistics are computed from this data stream and used to monitor and adjust the SSD.

Laser Amplifiers

1. Amplifier Staging

The final aperture of the Upgrade was determined by the decision to use 60 beams (for high irradiation uniformity) and the requirement of 30 kJ of UV energy on the target. The beam size was then set by the damage threshold of the sol-gel coating on the input lens of the final spatial filter. The OMEGA Upgrade will have a final IR aperture of 20 cm, a substantial increase over the 9-cm aperture of the original OMEGA system.

a. Rod-amplifier staging. The rod-amplifier staging was dictated by the energy needed to compensate for the beam splitting required to generate 60 beams from a single driver line and, as with other designs, by budgetary considerations. The splitting, performed in steps of 3x, 5x, and 4x (actually two steps of 2x), in that order, was chosen (instead of, say, 10x and 6x) because of the availability of high-quality polarizer/splitters, with <6x splitting, using thin-film technology. This particular ordering was chosen because it produced a system configuration that fits inside the existing LLE laser bay. In addition, the splitting matches the saturated gain of the rod amplifiers to the energy partition. For example, the saturated gain of the rod amplifiers minus the losses in the beamline's applicable segment nearly equals the split fraction. This holds for the five-way split before stage B (6 cm) and the four-way split before stage D (9 cm). The three-way split was placed first because it minimizes the total number of rod amplifiers needed.

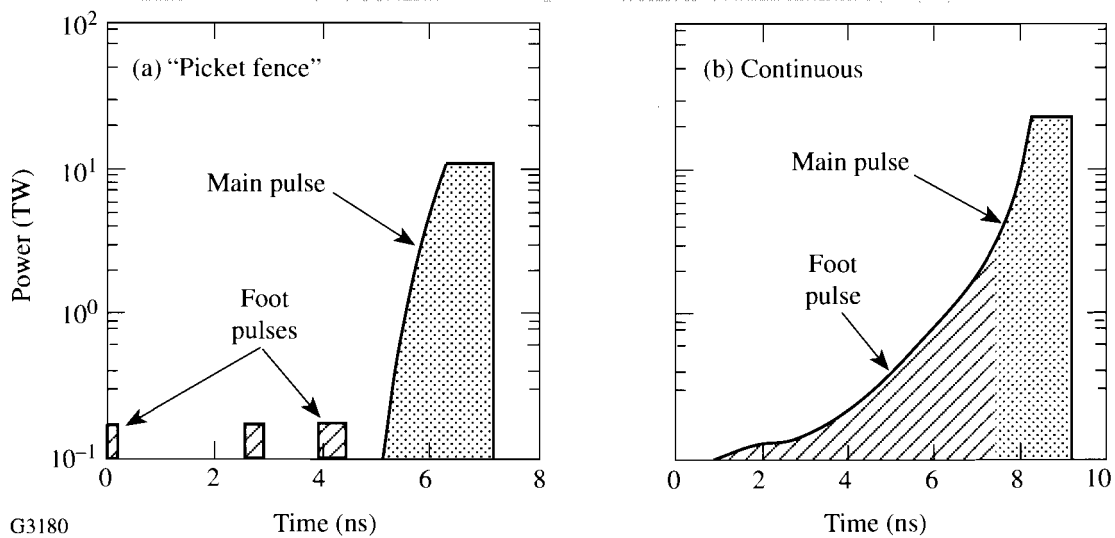
b. Power-amplifier staging. The final three amplifiers—a 9-cm rod, a 15-cm Brewster-disk amplifier, and a 20-cm disk amplifier—produce ~97% of the IR energy in each beamline. Moreover, nearly 90% of the system energy is in the main pulse, which has a temporal width in the range of 0.7 to 1.5 ns. The area ratios of the last stages are 1:2.78:5, a standard, short-pulse staging configuration entirely appropriate for the Upgrade's main-pulse performance. The penalty incurred for this staging is less-than-optimal performance for the foot pulse due to its longer pulse width (3–5 ns).

Several notable changes in staging have been made since the preliminary design. The original Galilean beam expander, between the 15- and 20-cm stages, has been changed to a standard spatial filter. This has the advantages of improving system longevity by filtering the beam, reducing the probability of optical ghosts, and easing the task of the optical system design by providing yet another image relay. Another important change having implications for system staging is a new baseline temporal pulse shape. The Title-I foot- and main-pulse shapes were essentially Gaussians (or for the foot, a Q-switched pulse shape). While these shapes will be used to initially validate system performance, ultimate operation will use newer, more complicated pulse shapes such as those shown in Fig. 56.32. Early fusion experiments will rely predominately on such pulse shapes.

For the continuous pulses the division between “foot” and “main” is more arbitrary than for the Gaussian pulses; this provides a level of flexibility in design. The frequency-conversion crystals now have a single thickness (instead of the “top-hat” design favored in the preliminary design) and are optimized for the main-pulse performance. The conversion-efficiency penalty incurred with the single-thickness crystals is mitigated by the freedom to change the area ratio of the foot and main pulses. Also, the additional cost and fabrication difficulty associated with top-hat crystals are avoided.

Fig. 56.32

Typical pulse shapes required for ignition-scaling experiments on the OMEGA Upgrade: (a) picket-fence pulse and (b) continuous pulse.



The B-integral is a measure of the phase retardation accumulated as a beam propagates through a medium possessing a nonlinear index of refraction. This phase retardation can cause self-focusing of optical noise in the beam, creating intensity modulations that can result in severe damage to a laser system. Spatial filtering removes these intensity modulations and essentially resets the wavefront distortion to an acceptable level. The laser designer is therefore concerned with the phase retardation accumulated between spatial filters, termed DB, which is typically kept below 2 rad. Moreover, practical constraints prohibit the complete elimination of phase retardation by the spatial filters. The resulting accumulation of residual retardation is termed SB. The effect of SB on laser performance is a complicated function of spatial frequencies and the estimates of optical noise in the system. The OMEGA Upgrade has SB's of 6.2 and 6.6 rad in the main and foot pulses, respectively, and no stage has a DB greater than 1.4 rad.

The energies, fluences, and B-integrals projected for the 39-TW version of the continuous pulse shape of Fig. 56.32 are shown in Figs 56.33 and 56.34. Typical of a medium-pulse-width (~1-ns) laser, the system performance is limited by damage fluence rather than by B-integral effects. It is expected that if DB rose to 2 rad, the nominal laser obscuration fractions (i.e., dirt) would yield a maximum spatial modulation of 1.8:1. Subsequent modeling has confirmed this expectation. All system fluences have been chosen such that the optical coatings can survive localized spikes in laser fluence 1.8 times higher than the average beam fluence. Recent experimental results indicate that if high cleanliness is maintained in the system, the 1.8:1 modulation is, indeed, conservative.

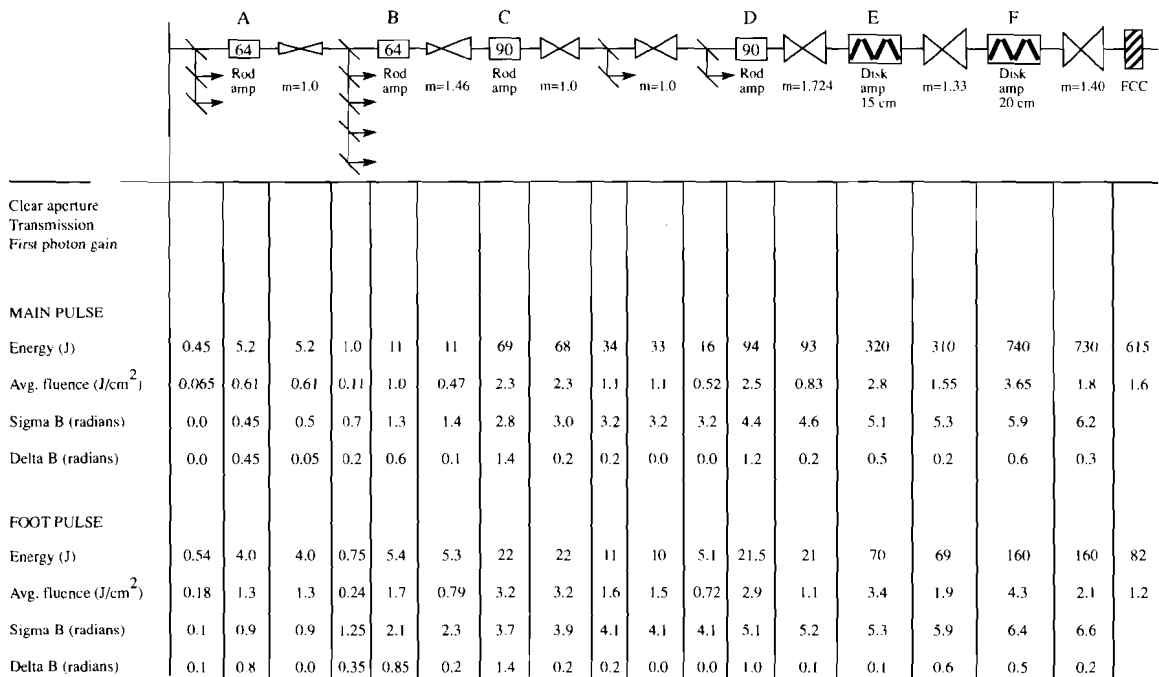


Fig. 56.33 Energy, fluence, ΣB and ΔB from the A amplifiers to the FCC's, for the main and foot pulses (39-TW continuous pulse shape).

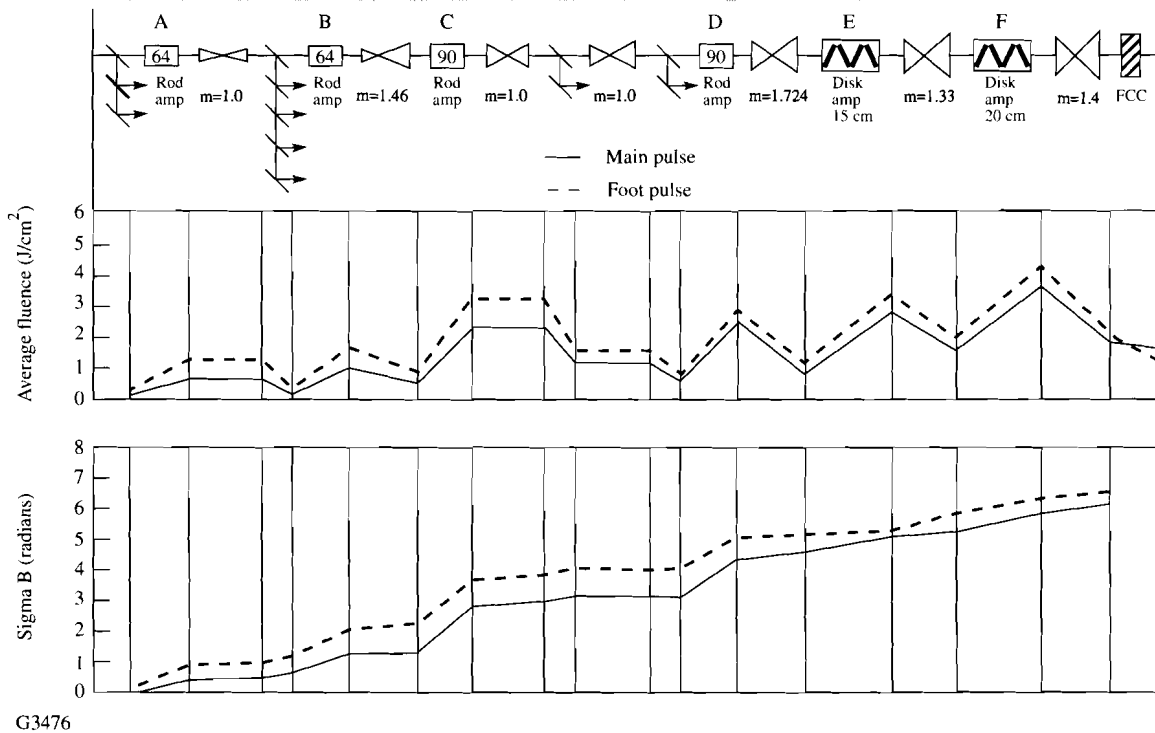


Fig. 56.34

Fluence and cumulative B-integral from the A amplifiers to the FCC's for the main and foot pulses (39-TW continuous pulse shape).

2. Rod Amplifiers

The ninety-four 64-mm and 90-mm rod amplifiers needed for the OMEGA Upgrade system will be fabricated from a design that reuses parts of the 54 amplifiers from the OMEGA system. Refinements to the original design have been implemented as a result of 12 years of experience using these amplifiers, and are aimed at improving performance, serviceability, and conformity to the rest of the system. The rod amplifier consists of a frame, a rod module, a pump module, and the various electrical and fluid connections. The rod-amplifier assembly is shown in Fig. 56.35.

The rod-amplifier frame is unchanged from the original design. The rod module has been redesigned to reduce the number of parts in order to cut cost and improve serviceability. The material used for all parts has been changed to improve resistance to corrosion by the deionized water/ethylene glycol solution used to cool the rods. The flow pattern for this coolant has been improved to provide more-uniform heat extraction, thereby reducing thermal stress in the rod.

The pump module, containing the flash lamps and reflectors, will utilize the same external shell, but the reflectors and flash-lamp assemblies have been changed. A new reflector configuration, a simple searchlight reflector geometry designed using the ZAP Monte Carlo ray-trace code,⁶ has been implemented to improve the cavity transfer efficiency. Prototype testing of this module will demonstrate the amount of increased performance of this design. The rod amplifiers use a 305-mm-arc-length, 300-Torr xenon flash lamp and the same connectors as used on the disk-amplifier pump modules. The flash-lamp assemblies

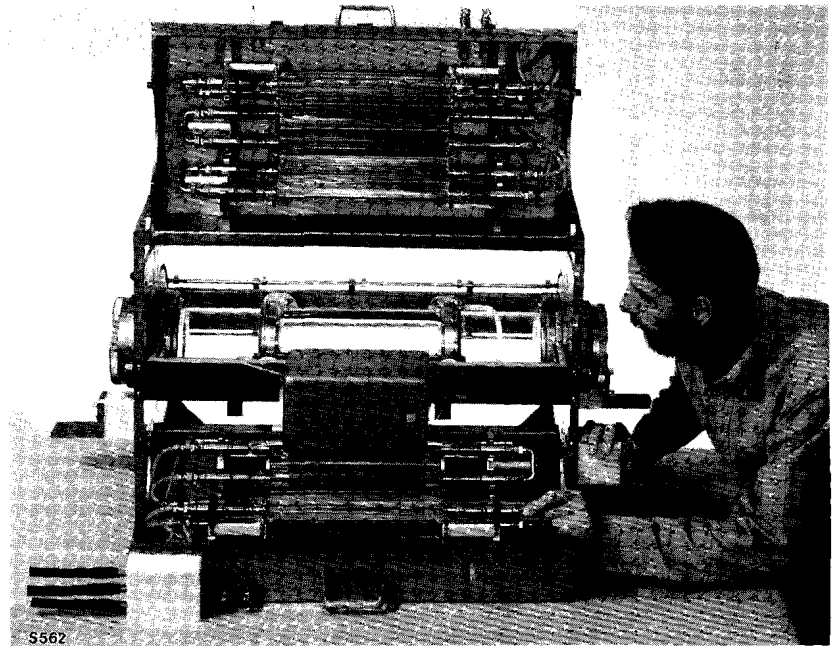


Fig. 56.35

The OMEGA-style rod amplifier used in the Upgrade. The pump modules (top and bottom) are open, showing the flash-lamp assemblies. These will be modified slightly to improve performance; the rod yoke assembly will be modified to improve reliability.

have also been redesigned to incorporate a configuration similar to the disk-amplifier bricks. The high-voltage connectors for the amplifier are to be identical to the ones used for the disk amplifiers.

The laser glass rods have been extended to 370 mm in length to accommodate improved O-ring seals. It was found that if the ends of the 90-mm rods were made parallel, an internal, end-to-end reflection would propagate unwanted energy just outside the laser aperture. To inhibit this reflection, the 90-mm rods will be finished with a 0.6-mrad wedge that prevents retroreflection within the rod.

3. Disk Amplifiers

The amplifiers for stages E and F are modern, 15- and 20-cm clear aperture, Nd:glass Brewster-disk amplifiers. The amplifiers are termed modern because they incorporate several unique features as well as a number of improvements suggested by others⁷ who have extensive experience in building disk amplifiers. These improvements include minimization of total amplifier volume⁸ for better coupling of pump light to the laser glass, transversely pumped rectangular design to avoid obscuration of flash lamps by disk supports,⁹ water-cooled flash lamps,¹⁰ and polymerically bonded edge cladding.¹¹

Each amplifier contains four Nd:phosphate glass (3-wt% doping), 3-cm-thick disks.¹² The number of disks was chosen to obtain adequate gain using the 3-cm-thick disks—a thickness chosen to minimize the B-integral. The pump pulse width was then optimized ($3\sqrt{LC} = 550 \mu\text{s}$) for high gain per unit path in the disks. Pump radiation is supplied by 19-mm-bore, water-cooled xenon flash lamps mounted on either side of the cavity.

Since the majority of the laser energy is in the relatively short (~1-ns) main pulse, an optimization of focusable power per amplifier dollar was more appropriate than total stored energy per amplifier dollar. The results of this optimization, plus a wavefront budget analysis for the system, yielded the

optical requirements for the 20- and 15-cm amplifiers that are summarized in Table 56.IV.

These requirements impose constraints on the mechanical and electrical design of the amplifier. As an example, the gain requirement results in pump-light fluences capable of incinerating any contamination within the amplifier. Since this could result in possible damage to the laser disks, high levels of cleanliness are required; these constraints are summarized in Tables 56.V and 56.VI.

A consistent and well-reasoned design philosophy is essential to meet all performance requirements and maintain safe design. To effect this, the philosophy addresses three aspects of the design: reliability, maintainability, and producibility.

The amplifiers have been designed for a 15-year, 20,000-shot lifetime. Reliability is driven by a number of factors such as system lifetime, maintenance intervals, and gain stability. Assuming one of the 120 disk amplifiers is maintained each week, the maintenance interval will be approximately 2.5 years. The degradation of the amplifier optical performance during this interval must be minimal.

Maintenance of the disk amplifiers has been approached in three ways: First, the amplifier must require minimal maintenance. Second, the most probable maintenance tasks (e.g., flash-lamp replacement) must be performed in place and be completed within a 60-min shot cycle. To facilitate this, the tools required must be minimal. Amplifiers are removed only for full maintenance or catastrophic failure. Third, repairs on subassemblies are conducted off-line, i.e., new assemblies are swapped in and the old ones repaired off-line.

Table 56.IV: Amplifier-performance optical requirements.

Clear aperture in centimeters	15	20
Number of disks per amplifier	4	4
Thickness per disk in centimeters	3.0	3.0
First-photon center-line gain	4.2	3.0
Gain uniformity across aperture	±10%	±10%
Average stored-energy density in J/cm^3 (assuming a stimulated emission cross section of $3.5 \times 10^{-20} cm^2$)	0.54	0.41
Cavity transfer efficiency	>1.14%	>1.14%
Nd ₂ O ₃ doping in wt%	3.0	3.0
$3\sqrt{LC}$ pump-pulse width, microseconds	550	550
Passive transmission	>96%	>96%
Wavefront, waves rms at 1054 nm	1	1
Repetition rate, shots per hour	1	1

Table 56.V: Mechanical requirements.

- Only organics that can survive intense UV irradiation
- Disk cavity isolated from the external environment
- Nitrogen purge for disk and pump cavities
- Maintainable on a 1-h shot cycle
- Class-100 compatibility a minimum, Class 10 a goal
 - permissible cleaning techniques
 - ultrasonic bath
 - high-pressure Freon or water spray
 - solvent wipe

Table 56.VI: Electrical requirements.

- Negligible contribution to 120-m Ω resistance budget of pulse-forming networks
- Materials compatible with deionized (18 M Ω •cm) water
- 40-kV dc standoff
- Electrically insulated in case of fault
- Provide ground plane for flash lamps

To ensure the amplifiers are produced in a cost-effective manner, considerable manufacturing engineering has been incorporated into the amplifier design. Conventional manufacturing methods that permit mass production have been used in addition to purchased parts whenever possible.

The 15- and 20-cm amplifiers consist of four major subassemblies: pump modules, flash-lamp bricks, disk-frame assemblies, and the amplifier-frame assembly. The 20-cm disk amplifier is depicted in Fig. 56.36. The amplifier frame supports the various other subassemblies. Hinged to the side of this frame are the pump modules that house the flash lamps and serve as the outer face of the optical cavity. The laser glass disks are mounted in disk-frame assemblies within the amplifier frame.

a. Amplifier-frame assembly. The frame assembly consists of seven major components that form the structural backbone of the amplifier. All components are machined from solid pieces of 6061-T6 aluminum, stress relieved and electroless nickel plated. The plating prevents oxidation and seals the exposed surfaces for operation in a class-100 clean area.

The amplifier frame design is nearly identical (except for scale) for the 15- and 20-cm amplifiers. The disk-frame assemblies kinematically mount within the frame assembly to avoid inducing stresses in the disk. The pump modules are held flush against the frame by spring-loaded hinges to minimize light leaks. Inside the frame the top, bottom, and ends of the optical cavity are constructed of separate, highly polished, silver-plated reflectors to maximize cavity transfer efficiency. The pump modules form the sides of the cavity and are separated from the laser glass by 6-mm-thick blast windows.

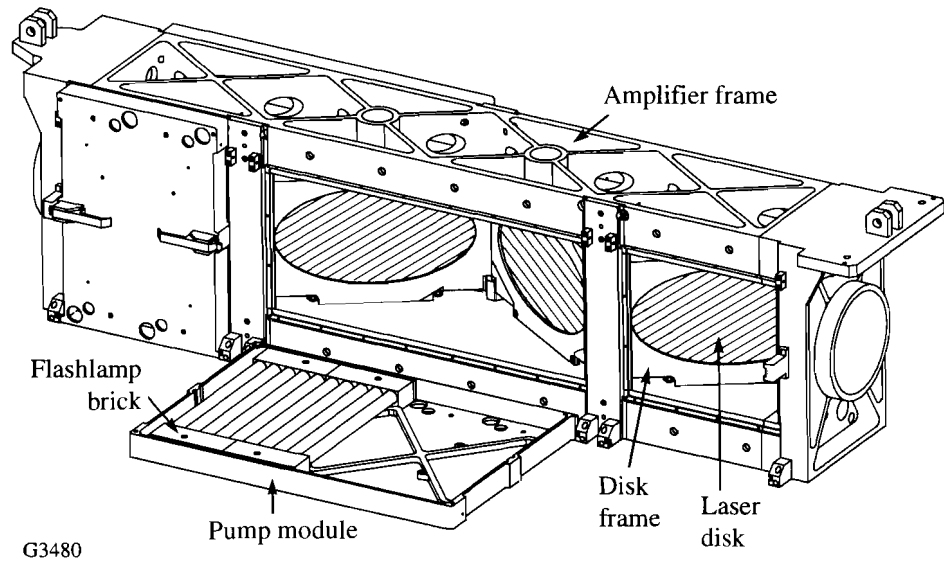


Fig. 56.36

The major components of the 20-cm disk amplifier for the OMEGA Upgrade. The 15-cm disk amplifier is a similar configuration (albeit smaller) but has longitudinal flash lamps rather than transverse.

Blast windows serve two functions in the amplifier design, which require class-100 clean-room conditions. First, they provide isolation from the class-1000 laser bay environment when the amplifier is opened for servicing. Secondly, the blast windows stop flash-lamp-generated acoustic disturbances that would degrade the transmitted wavefront quality.

b. Pump-module assemblies. The pump modules containing the flash-lamp bricks and reflectors have been specifically designed to permit *in-situ* replacement of flash-lamp-brick assemblies. A novel mechanical design with quick-release electrical and coolant connectors allows the replacement of a flash-lamp brick within the required 1-h shot cycle.

To maximize the cavity transfer efficiency the pump modules contain a highly polished, silver-plated, flat reflector placed within 1 mm of the flash-lamp water jacket. The proximity of this reflector provides the electrical ground plane essential for flash-lamp triggering. To prevent degradation of the silver surfaces, the pump modules are kept in a slightly pressured (<1-psi) nitrogen environment. As a secondary feature, the nitrogen environment reduces acoustic noise generation from the absorption of the lamp light in Schumann-Runge bands in oxygen between 175–195 nm.¹³

c. Flash-lamp-brick assembly. The disk amplifiers are pumped by (12) 1.32-m-arc-length or (80) 0.25-m-arc-length, 19-mm-bore, water-cooled xenon flash lamps. The flash lamps are mounted on 34-mm centers for a packing fraction of 1.75. The flash lamps are driven by (12) or (16) 19-kJ pulse-forming networks (PFN's). This results in total bank energies of 227 and 300 kJ at nominal bank voltage with the lamps operating at a 26% explosion fraction. These bank energies are based on 1.14% cavity transfer efficiency. The pulsed-power system also includes a pre-ionization lamp check (PILC).¹⁴ (See **Power Conditioning** in the next issue of the LLE Review.)

The flash-lamp-brick assembly consists of a flash lamp or group of flash lamps, their water jackets, the electrical connections, and water connections. For the 15-cm amplifier, a brick consists of a single flash-lamp assembly. Five flash-lamp assemblies are used in a brick for the 20-cm amplifier. In both cases, the total flash-lamp arc length is about 1.3 m. The five flash-lamp assemblies are connected in series electrically and for coolant flow.

Cooling with deionized (DI) water has a number of advantages. The DI water used in the closed-loop cooling system has a resistivity of 10–18 $M\Omega\cdot\text{cm}$. At this resistivity level the DI water serves as an electrical insulator.¹⁵ Water cooling has been demonstrated to improve flash-lamp reliability, especially when lamps are operated at higher fractions (20%–35%) of explosion energies. As opposed to air-cooled flash lamps, which fail in an explosive manner depositing glass and metallic debris over a large area, water-cooled flash lamps fail in a noncatastrophic manner—they simply fill with water. A catastrophic failure that generates debris is not acceptable for amplifiers operating in a class-100 environment.

Each flash-lamp assembly consists of a flash lamp, a water jacket, and two flash-lamp connectors. The flash-lamp assemblies are 300-Torr xenon flash lamps of either 1.3-m or 0.25-m arc length. To reduce UV emission, the flash-lamp envelopes (22×1.5 -mm tubes) are made of cerium-doped quartz (CDQ). Because metallic ions are highly soluble in DI water, the flash-lamp lugs are passivated 316 stainless steel. In addition, all components of the flash-lamp connector directly exposed to DI water are also made of 316 stainless steel. The remaining components of the flash-lamp connector are made of 20%-glass-reinforced Ultem¹⁶ to provide electrical insulation. The water jackets are made from 27×1.5 -mm Corning¹⁷ 7740 Pyrex tubing.

d. Disk-frame assemblies. Except for scale, the disk frames of the 15- and 20-cm amplifiers are identical. Each assembly has two pieces (frame and cover) machined from solid plates of 6061-T6 aluminum, stress relieved and silver plated. Care is taken to center the laser disks within the frame and to ensure a 5.1-psi, “continuous” elliptical ring contact on the laser glass surface. The metal-to-glass contact area never overlaps the laser glass to cladding glass bond line. Modeling of this design has shown that the induced Hertzian stresses¹⁸ decay outside the disk’s clear aperture.

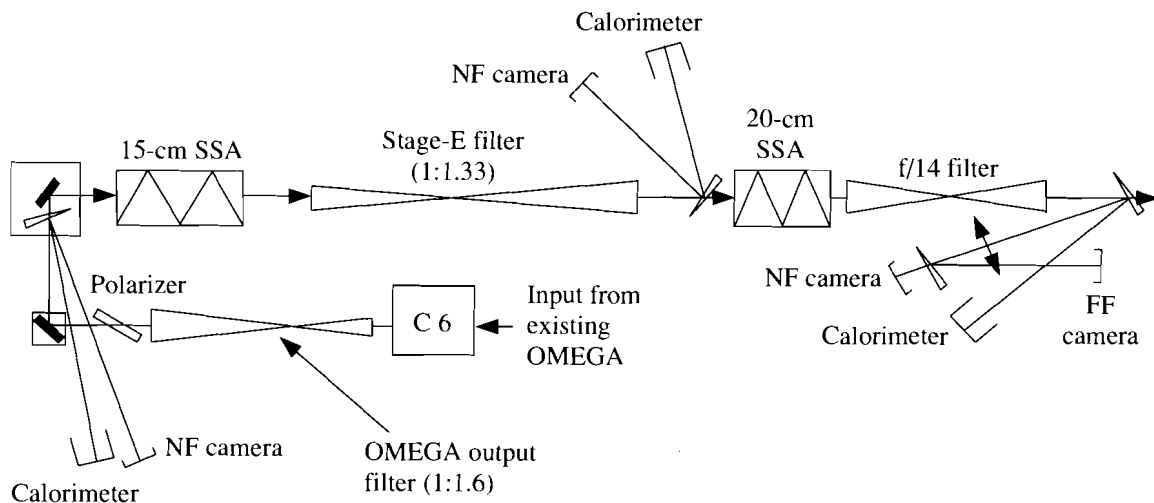
4. Amplifier Performance

In the upgraded system, 97% of the IR energy is produced after the last split, in the last three amplifiers. Because of the importance of this portion of the system and the relative ease of prototyping a simple chain without splits, a replica of this chain was constructed and its large-signal performance evaluated. These tests were conducted after an extensive series of small-signal measurements were performed on the disk amplifiers. The small-signal data so accumulated were necessary to compare the large-signal data to theory. Detailed comparisons between theory and experiment could then be made via simple Frantz-Nodvik models.¹⁹ The small-signal characterizations²⁰ will not be described here, but the results of these tests will be used freely to explain the large-signal results.

The large-signal performance was evaluated under specific conditions that

took advantage of existing drivers and eased interpretation of the results. The first condition was that the test beam was not co-propagated. In the final amplifier the aperture was filled with an 18-cm single beam. The temporal pulse shape was nominally a 740-ps-wide Gaussian from the mode-locked oscillator. Since advanced uniformity schemes require various types of modulation, testing was performed with transform-limited, 740-ps pulses, FM-modulated pulses with 5 Å of bandwidth and, finally, with spectrally dispersed, FM-modulated pulses used in the SSD scheme. The measurements included output energy versus input energy on a stage-by-stage basis, the passive losses per stage, and the near-field beam quality.

The test beamline is schematically shown in Fig. 56.37. A beam from the then-existing OMEGA system was picked off and injected into the prototype 15- and 20-cm amplifiers. A prototype of the spatial filter to be used on the Upgrade between stages E and F was placed between the amplifiers. Since a similar prototype of the Upgrade's output spatial filter was not available, a 21-cm-clear-aperture $f/14$ spatial filter (from LLNL) was used at the output. The acceptance angle of that final filter was chosen to be 800 mrad, half-width. This was primarily driven by pinhole closure considerations.²¹



G3375

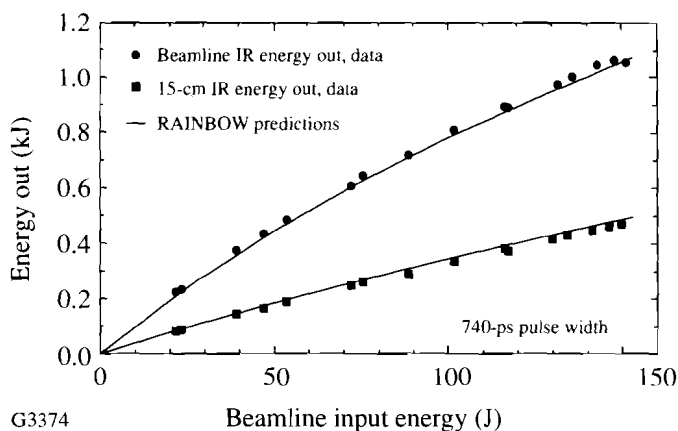
Fig. 56.37

The experimental setup for the demonstration of 1 kJ out of a single Upgrade beamline. The input was the 90-mm output of the original OMEGA system. Note that all diagnostics are after the spatial filters to insure measurement of only focusable energy.

The results of these tests are presented in Fig. 56.38, a plot of energy out of the test beamline for both 15- and 20-cm amplifiers versus drive energy from the 9-cm rod amplifier. The measurements were taken after a spatial filter to ensure that only focusable energy was measured. The Upgrade design goal is equivalent, in this simplified configuration, to a 1.0-kJ output with 140-J input; this was readily achieved. Also shown in Fig. 56.38 are the predictions of a simple Frantz-Nodvik¹⁹ calculation of the large-signal gain. In order to perform this calculation, the saturation fluence, small-signal gain, passive losses, and beam profiles were required. [Published values of the saturation fluence were used (nominal 3.75 J/cm²) with the two-ion model of Yarema and Milam.²²] Stage-

Fig. 56.38

The output energy of the beamline shown in Fig. 56.37 versus input energy. The goal of 1 kJ was reached at ~150-J input, thus assuring the energy performance of the OMEGA Upgrade.



by-stage passive losses were measured calorimetrically with the amplifiers unpumped. The beam profile was measured by taking near-field photographs on high-speed IR film and converting density to intensity. Small-signal gain was measured during the separate off-line characterization of each of the amplifiers; reasonable agreement was observed.

In addition to the energy-transport measurements, targeting-stability concerns dictated that a full-aperture, pointing-stability characterization be performed. In this measurement, the two disk-amplifier stages were double-passed by a full-aperture, Q-switched Nd:YAG beam. The double-passing was accomplished by placing a partially reflecting mirror at the output of the chain. The outgoing and return beams were imaged onto a far-field camera. The separation between the two resulting far-field spots is a measure of the effect the amplifiers have on beam pointing. Since the YAG was Q-switched, this measurement could be made just prior to firing the amplifiers and exactly at the gain peak, thereby providing a measure of the dynamic pointing that occurs during a shot. The result of these measurements indicated that the whole-beam steering in the horizontal direction due to firing of the disk amplifiers is less than $1 \mu\text{rad}$. It is expected that no steering will occur in the vertical direction.

5. Laser Glass

In keeping with the philosophy of using proven, low-risk technologies, LHG-8 laser glass²³ was chosen as the active medium for the Upgrade. It is a well-characterized, athermal phosphate laser glass that provides a high cross section for stimulated emission, extremely low $1\text{-}\mu\text{m}$ absorption, and a reduced nonlinear index of refraction when compared with the silicate glasses. LHG-8 can be melted in production quantities while maintaining sufficient homogeneity and low particulate platinum content.

Nd-doped phosphate glasses are known²⁴ to be susceptible to shortening of the lifetime of the upper lasing level due to multiphonon de-excitation by excess water in the glass melt. The minimum fluorescence lifetime is chosen to ensure that this effect is not a limiting factor in determining the amplifier performance.

The disk-cladding technology was developed at LLNL¹¹ utilizing a polymer bond to attach copper-doped LHG-8 glass to the disk edges in a stress-free manner. This cladding effectively reduces parasitic oscillations.

At the recommendation of LLE, the vendor utilized phase-shifting interferometry and polished-homogeneity-testing²⁵ technology to monitor the homogeneity of the production laser glass. This quality-control step assisted in the production of glass that exceeded the specifications for homogeneity. The specifications and work statements for the laser-glass procurement are contained in the design review package submitted for the KD3'. The selection and procurement of laser glass have been described elsewhere.¹²

6. Flash Lamps

The 217 laser amplifiers in the OMEGA Upgrade will require nearly 7,000 flash lamps. These units will be 19-mm-bore, 300-Torr, xenon flash lamps and will have arc lengths of 0.25, 1.32, and 0.3 m for the 20-cm SSA, 15-cm SSA, and rod amplifiers, respectively. Other than the arc length all features of the flash lamps are identical.

All of the OMEGA Upgrade flash lamps are water cooled, thus providing a number of advantages over air-cooled flash lamps: The lamps can be run at a higher explosion fraction. (This is the operational energy divided by the maximum energy a lamp can survive and not explode.) The Upgrade lamps are operated at 26%–34% explosion fraction, whereas air-cooled lamps are normally operated at 20%–25%. The blanket of deionized water used to cool the lamps has high resistivity, which eliminates electrical arcing. The water also provides mechanical support allowing the use of lower-cost, industry-standard, 1.5-mm-thick jackets rather than custom heavy-wall jackets favored on other laser systems. Lastly, water-cooled flash lamps increase the transfer of thermal energy out of the amplifier after a shot. Air-cooled lamps, which dissipate thermal energy by radiation, ultimately heat the laser glass after a shot; water cooling removes this heat without heating the laser glass.

Along with the visible light used to pump Nd lasers, xenon flash lamps produce large amounts of UV light. The solarization of phosphate laser glass when exposed to intense UV light is a problem in high-power-laser designs. In the design of prototype amplifiers for the OMEGA Upgrade, the desire to eliminate as much UV light as possible has led to the use of cerium-doped-quartz (CDQ) envelopes that absorb much of the UV radiation from the flash-lamp discharge. Recently, an additional attenuation of the UV radiation has been achieved using a new manufacturing process for the envelopes. The use of cerium-doped quartz and the new process for producing that quartz are the most significant improvements to these flash lamps relative to their predecessors.

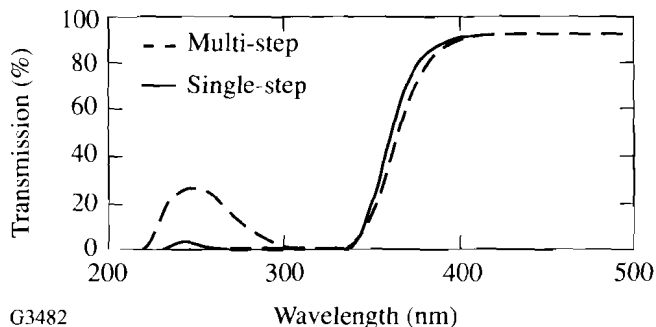
Originally, CDQ for flash lamps was manufactured using a multistep process. Quartz was produced using an oxygen/hydrogen flame, resulting in solid quartz ingots from which tubing for flash lamps was drawn. In the new, single-step process the raw material is melted in a crucible, and tubing is drawn directly from the bottom of the crucible. This process reduces the OH content of the quartz that

produces a concomitant reduction in the UV transmission of the quartz. Shown in Fig. 56.39 are the transmission curves for CDQ manufactured by the two processes. Note the marked reduction in the UV transmission and the virtually unchanged transmission in the visible band for the single-step process.

Table 56.VII shows a comparison of a few key parameters for the two manufacturing processes. The first three attributes favorably impact the performance and design, i.e., lower OH content, lower cost, and better tolerances. The last three attributes are primarily cosmetic in nature and are permitted, to some extent, without compromising flash-lamp performance.

Fig. 56.39

The output spectrum of the xenon flash lamps with cerium-doped quartz envelopes made with a multistep process (dashed) and a single-step process (solid). The newer, single-step process reduces unwanted UV radiation in the 250-nm range.



G3482

Table 56.VII: Comparison of single and multistep processes for producing cerium-doped quartz.

Attribute	Single-step Process	Multistep Process
OH content	80 ppm as drawn, vacuum anneal to < 8	130–220 ppm
Cost	Lower	Higher
Outside diameter and wall tolerances (mm)	$\pm 0.22/\pm 0.12$	$\pm 0.40/\pm 0.40$
Bubble content	Some	Minimal
Air lines (elongated bubbles)	Some	Minimal
Die and mandrel marks	Some	None

This completes the description of the subsystems of the OMEGA Upgrade Project, from Laser Drivers through Disk Amplifiers. In subsequent issues of the LLE Review, we shall provide the remainder of subsystems described in the Executive Summary. Subsystems yet to be described include Power Conditioning, Controls, Optomechanical Systems (both laser and target area), and Major Structures.

ACKNOWLEDGMENT

This work was supported by the U.S. Department of Energy Office of Inertial Confinement Fusion under Cooperative Agreement No. DE-FC03-92SF19460, the University of Rochester, and the New York State Energy Research and Development Authority.

REFERENCES

1. J. E. Murray and W. H. Lowdermilk, *J. Appl. Phys.* **51**, 3548 (1980).
2. J. E. Murray and D. J. Kuizenga, *Appl. Phys. Lett.* **37**, 27 (1980).
3. E. W. Roschger and J. E. Balmer, *Appl. Opt.* **24**, 3110 (1985).
4. S. Skupsky, R. W. Short, T. Kessler, R. S. Craxton, S. Letzring, and J. M. Soures, *J. Appl. Phys.* **66**, 3456 (1989).
5. D. L. Brown, I. Will, W. Seka, and M. Tracy, "Large-Aperture Ring Amplifier with Gains in Excess of 40,000 and Several-Joule Output Capability," presented at CLEO '93, Baltimore, MD, 2-7 May 1993; M. D. Tracy, I. Will, C. K. Merle, R. G. Roides, K. Thorp, M. D. Skeldon, J. H. Kelly, and W. Seka, "Versatile Front-End Laser System for Laser-Fusion Drivers," to be presented at the 1993 OSA Annual Meeting, Toronto, Canada, 3-8 October 1993.
6. The code used is a greatly updated and enhanced version of the code ZAP originally written by Systems, Science and Software for the Naval Research Laboratory by J. H. Alexander, M. Troost, and J. E. Welch, ARPA order number 660, Contract number N00014-70-C-0341, 1971.
7. We are grateful for the cooperation of our colleagues at Lawrence Livermore National Laboratory, especially Dr. H. T. Powell, Dr. J. E. Murray, and Dr. A. T. Erlandson.
8. J. Boon, C. Danson, and M. Mead, "φ108 Disc Amplifier Cooling," Rutherford Appleton Laboratory Annual Report to the Laser Facility Committee RAL-85-0047 (1985), pp. A6.6-A6.12.
9. S. M. Yarema and J. E. Murray, Lawrence Livermore National Laboratory Laser Program Annual Report 1980, UCRL 50021-80 (1981), pp. 2-234-2-244.
10. Private communication from K. Moncur, KMS Fusion (1989).
11. C. R. Wolfe, H. G. Patton, and H. T. Powell, Lawrence Livermore National Laboratory Laser Program Annual Report 1986, UCRL 50021-86 (1987), pp. 4-14-4-59.
12. M. J. Shoup III, S. D. Jacobs, J. H. Kelly, C. T. Cotton, S. F. B. Morse, and S. A. Kumpan, in *Solid State Lasers III* (SPIE, Bellingham, WA, 1992), Vol. 1627, pp. 192-201.
13. K. Wantanabe, E. C. Y. Inn, and M. Zelikoff, *J. Chem. Phys.* **21**, 1026 (1953).
14. A. C. Erlandson, Lawrence Livermore National Laboratory Laser Program Annual Report 1985, UCRL 50021-85 (1986), pp. 7-18-7-25.
15. M. Zahn *et al.*, *Proc. IEEE* **74**, 1182 (1986).
16. General Electric Company, One Plastics Avenue, Pittsfield, MA 01201. Reference to a company or a product name does not imply approval or recommendation of the product by the University of Rochester or the U.S. Department of Energy.

17. Corning Glass Works, Corning, NY 14830. Reference to a company or a product name does not imply approval or recommendation of the product by the University of Rochester or the U.S. Department of Energy.
18. W. C. Young, *Roark's Formulas for Stress & Strain*, 6th ed. (McGraw-Hill, New York, 1989), Chap. 13, pp. 647–665.
19. L. M. Frantz and J. S. Nodvik, *J. Appl. Phys.* **34**, 2346 (1963).
20. J. H. Kelly, M. J. Shoup III, M. M. Tedrow, and K. Thorp, "Energy Transport in a Modern Disk Amplifier," in *Solid State Lasers III* (SPIE, Bellingham, WA, 1992), Vol. 1627, pp. 286–297.
21. J. M. Auerbach, N. C. Holmes, J. T. Hunt, and G. J. Linford, *Appl. Opt.* **18**, 2495 (1979).
22. S. M. Yarema and D. Milam, *IEEE J. Quantum Electron.* **QE-18**, 1941 (1982).
23. Hoya Optics, Inc., 3400 Edison Way, Fremont, CA 94538-6190. Reference to a company or a product name does not imply approval or recommendation of the product by the University of Rochester or the U.S. Department of Energy.
24. C. B. Layne, Ph.D. Thesis, University of California, Davis, 1975.
25. A. Chiayu and J. C. Wyant, *Opt. Eng.* **30**, 1399 (1991).

PUBLICATIONS AND CONFERENCE PRESENTATIONS

Publications

S. Alexandrou, R. Sobolewski, C.-C. Wang, and T. Y. Hsiang, "Subpicosecond Electrical Pulse Generation in GaAs by Nonuniform Illumination of Series and Parallel Transmission-Line Gaps," in *OSA Proceedings on Ultrafast Electronics and Optoelectronics*, edited by J. Shah and U. Mishra (Optical Society of America, Washington, DC, 1993), Vol. 14, pp. 209–212.

C. Bamber, W. R. Donaldson, E. Linke, and A. C. Melissinos, "A Pulsed-Power Electron Accelerator Using Laser-Driven Photoconductive Switches," in *Advanced Accelerator Concepts*, edited by J. S. Wurtele (American Institute of Physics, New York, 1993), Vol. 279, pp. 802–806.

R. Betti, "Plasma Oscillations Induced by Tangentially Injected Neutral Beams," *Plasma Phys. Control. Fusion* **35**, 941 (1993).

R. Betti and J. P. Freidberg, "Destabilization of the Internal Kink by Energetic Circulating Ions," *Phys. Rev. Lett.* **70**, 3428 (1993).

X. D. Cao and C. J. McKinstrie, "Solitary-Wave Stability in Birefringent Optical Fibers," *J. Opt. Soc. Am. B* **10**, 1202 (1993).

H. Chen, B. Soom, B. Yaakobi, S. Uchida, and D. D. Meyerhofer, "Hot-Electron Characterization from K_{α} Measurement in High-Contrast, p -Polarized, Picosecond Laser-Plasma Interactions," *Phys. Rev. Lett.* **70**, 3431 (1993).

W. R. Donaldson and L. Mu, "Transmission-Line Modeling of Photoconductive Switches," in *Optically Activated Switching III*, edited by R. Aaron Falk (SPIE, Bellingham, WA, 1993), Vol. 1873, pp. 201–207.

- W. R. Donaldson and A. C. Melissinos, "A Novel High Brilliance Electron Source," in *Advanced Accelerator Concepts*, edited by J. S. Wurtele (American Institute of Physics, New York, 1993), Vol. 279, pp. 791–795.
- P. M. Fauchet, D. Hulin, A. Mourchid, and R. Vanderhaghen, "Ultrafast Thermal Nonlinearities in Amorphous Silicon," in *Ultrafast Laser Probe Phenomena in Bulk and Microstructure Semiconductors and High-Temperature Superconductors* (SPIE, Bellingham, WA, 1992), Vol. 1677, pp. 174–183.
- P. M. Fauchet, "Picosecond Spectroscopy in Solids with a FEL's," in *Spectroscopic Characterization Techniques for Semiconductor Technology IV* (SPIE, Bellingham, WA, 1992), Vol. 1678, p. 232 (invited paper).
- P. M. Fauchet and T. Gong, "Femtosecond Dynamics of Hot Carriers in GaAs," in *Ultrafast Laser Probe Phenomena in Bulk and Microstructure Semiconductors and High-Temperature Superconductors* (SPIE, Bellingham, WA, 1992), Vol. 1677, pp. 25–34 (invited paper).
- T. Gong, K. B. Ucer, L. X. Zheng, G. W. Wicks, J. F. Young, P. J. Kelly, and P. M. Fauchet, "Femtosecond Carrier-Carrier Interactions in GaAs," in *Ultrafast Phenomena VIII* (Springer-Verlag, 1993), pp. 402–404.
- T. Gong, L. X. Zheng, Y. Kostoulas, W. Xiong, W. Kula, K. B. Ucer, R. Sobolewski, and P. M. Fauchet, "Ultrafast Optical and Optoelectronic Response of Y-Ba-Cu-O," in the *OSA Proceedings on Ultrafast Electronics and Optoelectronics* (Optical Society of America, Washington, DC, 1993), Vol. 14, pp. 234–237.
- T. Gong, L. X. Zheng, W. Xiong, W. Kula, R. Sobolewski, P. M. Fauchet, J. P. Zheng, H. W. Kwok, and J. R. Gavaler, "Femtosecond Spectroscopy of Y-Ba-Cu-O Thin Films," in *AIP Conference Proceedings 273: Superconductivity and Its Applications* (American Institute of Physics, New York, 1993), pp. 327–335.
- J. W. Herman, H. E. Elsayed-Ali, and E. A. Murphy, "Time-Resolved Structural Study of Pb(100)," *Phys. Rev. Lett.* **71**, 400 (1993).
- S. D. Jacobs, D. Golini, A. Lindquist, B. Puchebner, M. J. Cumbo, A. Feltz, W. Czajkokowski, J. Greivenkamp, D. T. Moore, and H. M. Pollicove, "Technical Advances in Process Science Research at the Center for Optics Manufacturing," in *International Progress in Precision Engineering*, edited by N. Ikawa *et al.* (Butterworth & Heinemann, 1993), pp. 1046–1050.
- W. Kula and R. Sobolewski, "Influence of the Crystalline Structure of Critical Current Density in Bi(Pb)-Sr-Ca-Cu-O Thin Films Superconducting above 100 K," in *AIP Conference Proceedings 273: Superconductivity and Its Applications* (American Institute of Physics, New York, 1993), pp. 226–230.
- R. L. McCrory, J. M. Soures, J. P. Knauer, S. A. Letzring, F. J. Marshall, S. Skupsky, W. Seka, C. P. Verdon, D. K. Bradley, R. S. Craxton, J. A. Delettrez, R. Epstein, P. Jaanimagi, R. Keck, T. Kessler, H. Kim, R. L. Kremens, P. W. McKenty, R. W. Short, and B. Yaakobi, "Short-Wavelength-Laser Requirements for Direct-Drive Ignition and Gain," *Laser Part. Beams* **11**, 299 (1993).
- D. D. Meyerhofer, H. Chen, J. A. Delettrez, B. Soom, S. Uchida, and B. Yaakobi,

E. A. Murphy, H. E. Elsayed-Ali, and J. W. Herman, "Superheating of Bi(0001)," *Phys. Rev. B* **48**, 4921 (1993).

J. M. Soures, R. L. McCrory, T. R. Boehly, R. S. Craxton, S. D. Jacobs, J. H. Kelly, T. J. Kessler, J. P. Knauer, R. L. Kremens, S. A. Kumpan, S. A. Letzring, W. D. Seka, R. W. Short, M. D. Skeldon, S. Skupsky, and C. P. Verdon, "OMEGA Upgrade Laser for Direct-Drive Target Experiments," *Laser Part. Beams* **11**, 317 (1993).

W. Xiong, W. Kula, R. Sobolewski, and J. R. Gavaler, "Superconducting Properties of Laser-Annealed Lines Fabricated in Oxygen-Deficient Y-Ba-Cu-O Thin Films," in *AIP Conference Proceedings 273: Superconductivity and Its Applications* (American Institute of Physics, New York, 1993), pp. 433–436.

Forthcoming Publications

R. L. McCrory, J. M. Soures, C. P. Verdon, T. R. Boehly, D. K. Bradley, R. S. Craxton, J. A. Delettrez, R. Epstein, R. J. Hutchison, P. A. Jaanimagi, S. D. Jacobs, J. H. Kelly, R. L. Keck, T. J. Kessler, H. Kim, J. P. Knauer, R. L. Kremens, S. A. Kumpan, S. A. Letzring, F. J. Marshall, P. W. McKenty, S. F. B. Morse, W. Seka, R. W. Short, M. D. Skeldon, S. Skupsky, and B. Yaakobi, "Direct-Drive Laser Fusion Target Physics Experiments," to be published in the *Proceedings of the 14th International Atomic Energy Agency (IAEA) International Conference on Plasma Physics and Controlled Nuclear Fusion Research*, 30 September–7 October 1992, Wurzburg, Germany.

R. L. McCrory, "Progress Toward Ignition with Direct Drive," to be published in *Concerning Major Systems in Science and Technology*.

C. J. McKinstrie, X. D. Cao, and J. S. Li, "The Nonlinear Detuning of Four-Wave Interactions," to be published in the *Journal of the Optical Society of America B*.

D. D. Meyerhofer and J. Peatross, "Angular Distributions of High-Order Harmonics," to be published in *SILAP (Super-Intense Laser Atom Physics)*.

L. Mu and W. R. Donaldson, "Simulating Photoconductive Switches in a Microwave Transmission Line," to be published in the *Proceedings of the 9th IEEE International Pulsed Power Conference*, Albuquerque, NM, 21–23 June 1993.

J. Peatross and D. D. Meyerhofer, "Novel Gas Target for Use in Laser Harmonic Generation," to be published in *Review of Scientific Instruments*.

J. Z. Roach, A. Ninkov, S. W. Swales, and T. Morris, "Design and Evaluation of a Screen CCD Imaging System," to be published in *Optical Engineering*.

J. K. Samarabandu, R. Acharya, C. D. Edirisinghe, P. C. Cheng, H. Kim, T. H. Lin, R. G. Summers, and C. E. Musial, "Analysis of Multi-Dimensional Confocal Images," to be published in the *Proceedings of the SPIE Symposium "Biomedical Imaging"*, San Diego, CA, 24 February 1991.

N. Sampat, "Imaging System Design and Image Analysis Techniques for the Automatic Alignment of a Fusion Laser," to be published in the *Journal of Electronic Imaging*.

L. Shi, T. Gong, W. Xiong, X. Weng, Y. Kostoulas, R. Sobolewski, and P. M. Fauchet, "Femtosecond Reflectivity of 60-K Y-Ba-Cu-O Thin Films," to be published in *Applied Physics Letters*.

L. Shi and S.-H. Chen, "New Thermotropic Liquid Crystal Polymers Containing High Birefringence Cyanotolane Moiety," to be published in *Macromolecules*.

M. D. Skeldon and S. T. Bui, "Temporal Pulse-Width Control of a Regenerative Amplifier with Intracavity Etalons," to be published in the *Proceedings of SPIE's OE/LASE '93*, Los Angeles, CA, 16–23 January 1993.

S. Skupsky and T. J. Kessler, "Strategies for Ultra-High Laser Uniformity Using Zero-Correlation Phase Masks," to be published in the *Proceedings of SPIE's OE/LASE '93*, Los Angeles, CA, 16–23 January 1993.

S. Skupsky and T. J. Kessler, "A Speckle-Free Phase Plate (Diffuser) for Far-Field Applications," to be published in the *Journal of Applied Physics*.

R. Sobolewski, W. Xiong, W. Kula, and J. R. Gavalier, "Laser Patterning of Y-Ba-Cu-O Thin-Film Circuits," to be published in *Applied Physics Letters*.

R. Sobolewski, W. Xiong, W. Kula, and B. McIntyre, "Electrical and Structural Properties of the YBCO Superconducting-Semiconducting Interface," to be published in *Physica B*.

B. Soom, H. Chen, Y. Fisher, and D. D. Meyerhofer, "Strong K_{α} Emission in Picosecond Laser-Plasma Interactions," to be published in the *Proceedings of Short Wavelength V: Physics with Intense Laser Pulses ('93)* (an OSA proceedings).

B. Soom, H. Chen, Y. Fisher, and D. D. Meyerhofer, "Strong K_{α} Emission in Picosecond Laser-Plasma Interactions," to be published in the *Journal of Applied Physics*.

J. M. Soures, "Solid State Lasers," to be published in *Nuclear Fusion by Inertial Confinement*, edited by G. Velerade, Y. Ronen, and J. M. Martinez-Val.

J. M. Soures, "High-Technology Advances from LLE Research," to be published in the *Rochester Business Profiles Journal*.

J. M. Soures, "The OMEGA Upgrade Laser Facility for Direct-Drive Experiments," to be published in the *Proceedings of the Fusion Power Associates Annual Meeting and Symposium*, Princeton, NJ, 25–26 June 1991, and in the *Journal of Fusion Energy*.

J. Sweetser, T. J. Dunn, I. A. Walmsley, C. Radzewicz, S. Palese, and R. J. D. Miller, "Characterization of an FM Mode-Locked Nd:YLF Laser Synchronized with a Passively Mode-Locked Dye Laser," to be published in the *Journal of the Optical Society of America B*.

C. J. Twomey, S. H. Chen, T. Blanton, A. W. Schmid, and K. L. Marshall, "Solid Polymers Doped with Rare Earth Metal Salts. II. Thermal Behavior and

Morphology of the Neodymium Acetate-Poly(ethylene oxide) System,” to be published in the *Journal of Polymer Science, Polymer Physics Edition*.

C. J. Twomey, S.-H. Chen, T. Blanton, A. W. Schmid, and K. L. Marshall, “Solid Polymers Doped with Rare Earth Metal Compounds. III. Formation and Stability of Macromolecular Complexes Comprising Neodymium Nitrate and Dipivaloylmethane in Poly(Ethylene Oxide),” to be published in the *Journal of Polymer Science, Polymer Physics Edition*.

M. D. Wittman, R. Q. Gram, H. Kim, C. K. Immesoete, S. G. Noyes, and S. Scarantino, “Increased Retention Time for Hydrogen and Other Gases by Polymer Shells Using Optically Transparent Aluminum Layers,” to be published in the *Journal of Vacuum Science and Technology*.

W. Xiong, W. Kula, and R. Sobolewski, “Fabrication of High Superconducting Electronic Devices Using the Laser-Writing Patterning Technique,” in *Advances in Cryogenic Engineering*, Volume 40.

M. Yu, C. J. McKinstrie, and G. P. Agrawal, “Instability Due to Cross-Phase Modulation in the Normal Dispersion Regime,” to be published in *Physical Review E*.

X. Zhou, S. Alexandrou, and T. Y. Hsiang, “Monte Carlo Investigation of the Mechanism of Subpicosecond Pulse Generation by Nonuniform Gap Illumination,” to be published in *Applied Physics Letters*.

Conference Presentations

The following presentations were made at the Ninth Target Fabrication Specialists Meeting, Monterey, CA, 5–9 July 1993:

D. S. Brennan, “Modification of Carbon-Fiber Geometry Using an Oxygen-Plasma Etcher.”

R. Q. Gram, D. S. Brennan, S. G. Noyes, R. A. Mangano, and R. L. Fagaly, “A Low-Mass Mounting Method for Cryogenic Targets.”

H. Kim, “Fabrication of Ablator-Layer-Overcoated Foam Shells at Osaka University.”

S. G. Noyes, “Fabrication of Thin Planar Discs for Use in Long-Scale-Length Plasma Experiments.”

M. D. Wittman, “Compensation of the Lens Effects of Thick Cryogenic Layers Using an Interferometric Imaging System.”

The following presentations were made at the International Cryogenic Engineering Conference, Albuquerque, NM, 12–16 July 1993:

D. Gupta, W. R. Donaldson, and A. M. Kadin, “A Laser-Triggered, Inductive Opening Switch Using High-Temperature Superconducting Thin Films.”

W. Kula and R. Sobolewski, "Electric-Field-Effect Devices Based on Partially Oxygen-Depleted, Superconducting Y-Ba-Cu-O Thin Films."

W. Xiong, W. Kula, and R. Sobolewski, "Fabrication of High- T_c Superconducting Electronic Devices Using the Laser-Writing Patterning Technique."

The following presentations were made at ISEC '93, Boulder, CO, 12–14 July 1993:

T. Y. Hsiang, C.-C. Wang, A. Denysenko, S. Alexandrou, and R. Sobolewski, "An Electro-Optic Sampling System for Ultrafast Testing of Superconducting Circuits."

R. Sobolewski, W. Xiong, W. Kula, W. N. Maung, and D. P. Butler, "Monolithic Y-Ba-Cu-O Electronic Devices Fabricated Using the Laser-Writing Patterning Technique."

The following presentations were made at the XX International Conference on Low-Temperature Physics, Eugene, OR, 4–11 August 1993:

W. Kula and R. Sobolewski, "Electric-Field Effect in Partially Deoxygenated YBCO Thin Films."

R. Sobolewski, W. Xiong, W. Kula, and B. McIntyre, "Electrical and Structural Properties of the YBCO Superconducting-Semiconducting Interface."

The following presentations were made at the Eighth International Conference on Hot Carriers in Semiconductors (HCIS-8), Oxford, UK, 16–20 August 1993:

T. Gong, P. M. Fauchet, J. F. Young, G. W. Wicks, and P. J. Kelly, "Hot Carrier Dynamics Near the Fermi Edge."

Y. Kostoulas, T. Gong, and P. M. Fauchet, "Determination of Carrier-Carrier Scattering by a New Time-Resolved Technique."

J. F. Young, T. Gong, P. J. Kelly, and P. M. Fauchet, "Electron-Electron Scattering within Nonthermal Distributions."

W. I. Kordonsky, I. V. Prokhorov, G. Gorodkin, S. D. Jacobs, B. Puchebner, and D. Pietrowski, "Magnetorheological Finishing of Optics," 2nd Annual Symposium of the University of Rochester Chapter of the Materials Research Society (SOMR 93), Rochester, NY, 23 August 1993.

ACKNOWLEDGMENT

The work described in this volume includes current research at the Laboratory for Laser Energetics, which is supported by New York State Energy Research and Development Authority, the University of Rochester, the U.S. Department of Energy Office of Inertial Confinement Fusion under Cooperative Agreement No. DE-FC03-92SF19460, and other agencies.

UNIVERSITY OF
ROCHESTER